The Astrophysical Journal, 646:1070–1085, 2006 August 1

THE EVOLUTION OF OUTFLOW-ENVELOPE INTERACTIONS IN LOW-MASS PROTOSTARS

Héctor G. Arce[1]
Department of Astrophysics, American Museum of Natural History, Central Park West at 79th Street, New York, NY 10024; harce@amnh.org

and

Anneila I. Sargent
Division of Physics, Mathematics, and Astronomy, California Institute of Technology, Mail Stop 105-24, Pasadena, CA 91125; afs@astro.caltech.edu
Received 2005 October 21; accepted 2006 April 13

ABSTRACT

We present multiline and continuum observations of the circumstellar environment within 10^4 AU of a sample of protostars to investigate how the effects of outflows on their immediate environment change over time. ^{12}CO (1–0) emission probes the high-velocity molecular outflows near the protostars and demonstrates that the outflow opening angle widens as the nascent star evolves. Maps of the ^{13}CO (1–0) and HCO^+ (1–0) outflow emission show that protostellar winds erode the circumstellar envelope through the entrainment of the outer envelope gas. The spatial and velocity distribution of the dense circumstellar envelope, as well as its mass, is traced by the C^{18}O (1–0) emission and also displays evolutionary changes. We show that outflows are largely responsible for these changes and propose an empirical model for the evolution of outflow-envelope interactions. In addition, some of the outflows in our sample appear to affect the chemical composition of the surrounding environment, enhancing the HCO^+ abundance. Overall, our results confirm that outflows play a major role in the star formation process through their strong physical and chemical impacts on the environments of the young protostars.

Subject headings: ISM: evolution — ISM: jets and outflows — ISM: molecules — stars: formation — stars: pre–main-sequence

1. INTRODUCTION

Young stellar objects (YSOs) ranging in age from approximately 10^3 yr to more than 10^6 yr are known to power outflows that entrain the surrounding gas of the parent molecular cloud. Protostellar winds originate close to the surface of the forming star and must interact with the dense envelope surrounding the protostar-disk system (e.g., Königl & Pudritz 2000; Shu et al. 2000). These circumstellar envelopes, with sizes of 10^3–10^4 AU, are the primary mass reservoirs for YSOs. As a result, perturbations caused when outflow momentum and energy are injected into the protostellar surroundings can have a major impact on the mass assembly process. In fact, outflows are most likely to be responsible for the clearing of material from the protostellar surroundings, a process that could result in the termination of the infall phase (e.g., Velusamy & Langer 1998) and affect the star formation efficiency in the cloud (e.g., Matzner & McKee 2000). However, there is still no general understanding of how the outflow's effect on its immediate surroundings changes as the protostar evolves, as studies of the outflow-envelope interaction have been limited to a few specific cases.

In the nearest star-forming regions, circumstellar envelopes around low-mass YSOs have angular sizes of about 10″–30″. A detailed study of the outflow impact on the envelope requires observations that distinguish between the various velocity patterns that can exist in different density regimes in these envelopes (i.e., infall, outflow, rotation, and turbulence). Observations at high angular and velocity resolution of a variety of molecular species that trace a range of density and kinematic regimes are therefore essential. Also, in order to examine how the outflow-envelope interaction evolves, observations of the environment around protostars of different ages are needed.

Here we present the results of a systematic survey of the circumstellar environments of a sample of YSOs with outflows. Multiline and continuum high spatial and spectral resolution observations from the Owens Valley Radio Observatory (OVRO) millimeter-wave array enable investigation of the outflows, circumstellar gas, and evolution of the outflow-envelope interactions, on scales of $\sim 10^3$ AU. Considerably more detailed studies of two of the sources in our sample, L1228 and RNO 43, have already been published (Arce & Sargent 2004, 2005, hereafter Paper I and Paper II, respectively).

2. THE SAMPLE

Our observed sample consists of nine low-mass protostars at different evolutionary stages and includes (1) three Class 0 sources—deeply embedded protostars in the earliest formation stage, with ages between $\sim 10^3$ and $\sim 10^4$ yr (see André et al. 2000); (2) three Class I sources—protostellar objects still embedded in their parent cores but older than the Class 0 sources, with ages $\sim 10^5$ yr (see Lada 1999), and (3) three Class II sources, with ages of a $\sim$few $\times 10^6$ yr (Lada 1999). All are within 500 pc of the Sun and are known outflow sources, based on either millimeter or optical observations. Approximate protostellar ages are obtained from the bolometric temperature, $T_{\rm bol}$, the temperature of a blackbody having the same mean frequency as the observed spectral energy distribution (SED) of the YSO (see Myers & Ladd 1993; Chen et al. 1995; Ladd et al. 1998). Sources in our sample have $T_{\rm bol}$ ranging from 40 to 2700 K, corresponding to ages from $\sim 10^3$ to $\sim 10^7$ yr. Table 1 lists the

[1] NSF Astronomy and Astrophysics Postdoctoral Fellow.

TABLE 1
OBSERVED SOURCES

SOURCE NAME	ALTERNATE NAME	OBSERVATION COORDINATES		d	CLASS	T_{bol}[a]	SED REFERENCES[b]
		R.A. (2000.0)	Decl. (2000.0)	(pc)		(K)	
HH 114mms	...	5 18 15.4	7 12 00	460	0	40	1
IRAS 05295+1247	RNO 43	5 32 19.4	12 49 42	460	0	40	2, 3
IRAS 03282+3035	IRAS 3282	3 31 21.0	30 45 31	350	0	50	2, 4, 5
IRAS 04239+2436	HH 300	4 26 56.3	24 43 36	140	I	225	2, 5, 6, 7
IRAS 20582+7724	L1228	20 57 13.0	77 35 47	200	I	345	2, 7, 8
IRAS 21004+7811	RNO 129	20 59 13.8	78 23 05	200	I	650	2, 7
IRAS 16316−1540	RNO 91	16 34 29.3	−15 47 01	160	II	715[c]	2, 7, 9
T Tau	...	4 21 59.4	19 32 07	140	II	1235	2, 7, 9, 10, 11, 12, 13
GK/GI Tau[d]	...	4 33 34.4	24 21 07	140	II	2700[c]	7, 9

NOTE.—Units of right ascension are hours, minutes, and seconds, and units of declination are degrees, arcminutes, and arcseconds.

[a] Bolometric temperature calculated from spectral energy distribution following Chen et al. (1995) and combining our new observations with published data. Note that for T Tau, the flux measurements used do not resolve the individual components (see Appendix A.8).

[b] References used to obtain spectral energy distribution for each source: (1) Chini et al. 1997; (2) IRAS Catalog of Point Sources; (3) Zinnecker et al. 1992; (4) Dent et al. 1998; (5) Motte & André 2001; (6) Myers et al. 1987; (7) 2MASS All-Sky Catalog of Point Sources; (8) Arce & Sargent 2004; (9) Herbig & Bell 1988; (10) Weintraub et al. 1987; (11) Weintraub et al. 1989a; (12) Beckwith et al. 1990; (13) Beckwith & Sargent 1991.

[c] Bolometric temperature used here was taken directly from Chen et al. 1995.

[d] GK Tau and GI Tau are less than 15″ apart, and both are inside our field of view.

source names, coordinates of the observed fields, and other relevant parameters. A brief description of each source is given in the Appendix.

3. OBSERVATIONS

The observations were carried out using the OVRO millimeter array of six 10.4 m telescopes, during three observing seasons between 2001 September and 2004 May. For all sources in our sample, a single pointing (i.e., no mosaicking) and two different correlation configurations were used to provide images on a total of six different molecular lines and two 4 GHz–wide continuum emission bands. The area on the sky covered by each map is the OVRO primary beam, $65'' \times (100/\nu)$ (FWHM), where ν is the observed frequency in GHz.

The first digital correlator configuration provided simultaneous measurements of ^{12}CO (1–0), ^{13}CO (1–0), and C^{18}O (1–0) at 115.27, 110.20, and 109.78 GHz, respectively, and 4 GHz bandwidth continuum emission at 2.7 mm. With the local oscillator (LO) frequency set to 112.736 GHz, the ^{12}CO line was observed in the upper sideband with a channel width of 0.325 km s^{-1} over a 20 km s^{-1} bandwidth. In the lower sideband, the ^{13}CO and C^{18}O lines were each observed at a velocity resolution of 0.17 km s^{-1} over a 5 km s^{-1} bandwidth. Observations were obtained in two to five different array configurations, depending on the source, and with baselines extending from 15 m to a maximum of 480 m.

Simultaneous observations of HNC (1–0) $F = 2$–1, HCO$^+$ (1–0), and H^{13}CO$^+$ (1–0) at 90.66, 89.19, and 86.75 GHz, respectively, and of 4 GHz bandwidth continuum emission centered at 3.4 mm were obtained with the LO frequency tuned to 87.971 GHz, so that the HNC and HCO$^+$ lines were in the upper sideband and H^{13}CO$^+$ in the lower. All three lines were observed with two or three different array configurations with spectral resolutions of ~0.1 km s^{-1} over bandwidths of 6 km s^{-1}, and baselines from 15 m to a maximum of 120 m. Only maps of the HCO$^+$ emission are discussed here, as they are relevant to the present discussion.

A bright (>1 Jy) quasar near each observed source was used for phase and gain calibration. Flux calibration relied on observations of 3C 273 and Uranus, with resulting uncertainties of about 20%–30%. Visibility data were edited and calibrated using the MMA software package (Scoville et al. 1993), and images were produced using the MIRIAD software package (Sault et al. 1995) and its CLEAN algorithm, with "robust" weighting of the visibilities. For each map the robust parameter was chosen to optimize both spatial resolution and sensitivity to extended structures, as well as the signal-to-noise ratio. Table 2 provides a list of the relevant parameters for the molecular line and continuum emission data.

4. RESULTS

The gas surrounding forming stars is generally characterized by complex kinematics and steep density gradients, and observations of different molecular lines are necessary to trace different density and kinematic regimes. We use the optically thin 3 mm dust continuum emission to pinpoint the position of the sources in our sample and to study the inner circumstellar environment. The ^{12}CO (1–0) emission probes the low-density, high-velocity outflow gas, while the less optically thick ^{13}CO (1–0) emission reflects the behavior of the low-velocity, slightly denser outflow, as well as the impact of the protostellar outflow on the outer regions ($\gtrsim$2000 AU) of the circumstellar envelope. Observations of the C^{18}O (1–0) line trace the inner dense parts of the envelope surrounding the protostar and in some cases may be used to probe the effect of the outflow on the high-density gas. We originally observed HCO$^+$ (1–0) with the expectation that this would trace infall motions of the gas surrounding the young stars. Since HCO$^+$ (1–0) kinematics appears to be dominated by outflow motions, we have used these results to examine the physical and chemical impact of the outflow on the surrounding gas.

4.1. *Continuum Emission*

Millimeter continuum thermal dust emission at 2.7 and 3.4 mm was detected toward all the sources in our sample. Maps of this continuum emission were constructed so that both bands had similar synthesized beams (see Table 2). Since the linear resolution of our continuum observations ranges from about 700 to 2700 AU, it is very probable that both the emission from the envelope around the protostar and that from an unresolved

TABLE 2
CHARACTERISTICS OF LINE AND CONTINUUM MAPS

Line	Beam Size (arcsec)	Map rms[a] (Jy beam^{-1})	Line/Continuum	Beam Size (arcsec)	Map rms[a] (Jy beam^{-1})
			HH 114mms		
^{12}CO (1–0).....	4.3 × 3.9	0.08	HCO^+ (1–0)	6.4 × 5.4	0.11
^{13}CO (1–0).....	5.1 × 5.0	0.09	2.7 mm continuum	6.4 × 5.9	0.003
C^{18}O (1–0).....	5.3 × 4.9	0.07	3.4 mm continuum	6.3 × 6.1	0.0007
			RNO 43		
^{12}CO (1–0).....	4.4 × 4.0	0.10	HCO^+ (1–0)	5.4 × 5.2	0.13
^{13}CO (1–0).....	5.1 × 4.1	0.10	2.7 mm continuum	5.1 × 5.0	0.0007
C^{18}O (1–0).....	4.7 × 4.1	0.08	3.4 mm continuum	5.6 × 4.6	0.0004
			IRAS 3282		
^{12}CO (1–0).....	3.5 × 2.9	0.06	HCO^+ (1–0)	6.4 × 5.9	0.13
^{13}CO (1–0).....	4.9 × 4.1	0.08	2.7 mm continuum	4.3 × 4.0	0.001
C^{18}O (1–0).....	3.8 × 3.4	0.06	3.4 mm continuum	5.0 × 4.0	0.0006
			HH 300		
^{12}CO (1–0).....	4.4 × 3.2	0.07	HCO^+ (1–0)	6.9 × 6.6	0.11
^{13}CO (1–0).....	4.6 × 3.3	0.10	2.7 mm continuum	4.8 × 3.7	0.0008
C^{18}O (1–0).....	4.7 × 3.5	0.06	3.4 mm continuum	4.8 × 3.8	0.0004
			L1228		
^{12}CO (1–0).....	4.3 × 3.8	0.08	HCO^+ (1–0)	7.1 × 6.6	0.11
^{13}CO (1–0).....	4.8 × 4.0	0.07	2.7 mm continuum	6.0 × 5.7	0.0006
C^{18}O (1–0).....	4.7 × 3.9	0.08	3.4 mm continuum	6.3 × 5.5	0.0004
			RNO 129		
^{12}CO (1–0).....	5.7 × 4.4	0.11	HCO^+ (1–0)	8.5 × 5.3	0.10
^{13}CO (1–0).....	6.4 × 5.0	0.10	2.7 mm continuum	7.9 × 6.9	0.002
C^{18}O (1–0).....	6.8 × 5.7	0.08	3.4 mm continuum	9.1 × 6.0	0.0007
			RNO 91		
^{12}CO (1–0).....	6.2 × 4.5	0.16	HCO^+ (1–0)	11.7 × 6.3	0.25
^{13}CO (1–0).....	6.1 × 4.9	0.15	2.7 mm continuum	6.6 × 4.7	0.001
C^{18}O (1–0).....	6.6 × 5.0	0.12	3.4 mm continuum	13.3 × 7.8	0.0009
			T Tau		
^{12}CO (1–0).....	3.4 × 3.0	0.08	HCO^+ (1–0)	5.2 × 4.5	0.12
^{13}CO (1–0).....	3.7 × 3.6	0.09	2.7 mm continuum	4.6 × 4.3	0.002
C^{18}O (1–0).....	4.3 × 3.8	0.06	3.4 mm continuum	4.9 × 4.1	0.0005
			GK Tau		
^{12}CO (1–0).....	5.9 × 4.4	0.10	HCO^+ (1–0)	5.3 × 4.1	0.16
^{13}CO (1–0).....	7.0 × 6.1	0.12	2.7 mm continuum	7.1 × 5.3	0.0008
C^{18}O (1–0).....	6.9 × 5.7	0.09	3.4 mm continuum	6.4 × 6.1	0.0004

[a] In line maps, the rms per velocity channel is shown.

circumstellar disk contribute to the total detected emission. We expect that in the Class 0 sources more than 80% of the emission comes from the inner (<2000 AU) circumstellar envelope. For the Class I and II sources, we expect the contribution from the disk to the total detected emission to rise from about 30%–90% as the source evolves (e.g., Hogerheijde et al. 1997a; Looney et al. 2000).

We estimate the total mass of the gas and dust associated with the continuum emission, $M_{\rm cont}$, from $F_\nu D^2/B_\nu(T_d)\kappa_\nu$ (e.g., Beckwith et al. 1986). Here F_ν is the continuum flux density at frequency ν, D is the distance to the source, B_ν is the blackbody (Planck) function, T_d is the dust temperature, and κ_ν is the dust mass opacity coefficient, with the usual form, $\kappa_\nu = 0.1(\nu/10^{12}\ {\rm Hz})^\beta\ {\rm cm^2\ g^{-1}}$ (e.g., Beckwith & Sargent 1991). The value of β was determined by fitting the measured flux densities at wavelengths between 0.62 and 3.4 mm with a power law, $F_\nu \propto \nu^{(2+\beta)}$, using measurements from our observations and the literature (see references in Table 1). For sources with fewer than three available flux measurements, we adopt $\beta = 1$. The dust temperature was estimated from graybody fits to the SED of the source (e.g., Chini et al.

TABLE 3
CONTINUUM RESULTS

Source	R.A. (2000.0)	Decl. (2000.0)	$F_{2.7}$[a] (mJy)	$F_{3.4}$[a] (mJy)	β[b]	T_d[c] (K)	$M_{\rm cont}$[d] ($M_\odot$)
HH 114mms	5 18 15.2	7 12 02	110 ± 20	57 ± 11	0.4 ± 0.2	30	0.24
RNO 43	5 32 19.4	12 49 41	26 ± 6	11 ± 2	1.0 ± 0.1	35	0.19
IRAS 3282	3 31 20.9	30 45 30	61 ± 12	30 ± 6	0.76 ± 0.2	28	0.17
HH 300	4 26 56.3	24 43 35	14 ± 2	8 ± 2	1.5 ± 0.4	40	0.02
L1228	20 57 12.9	77 35 44	45 ± 9	21 ± 4	1.2 ± 0.4	33	0.10
RNO 129	20 59 13.6	78 23 03	62 ± 13	28 ± 6	1.0	40	0.07
RNO 91	16 34 29.3	−15 47 01	8 ± 2	3 ± 0.5	1.0	50	0.005
T Tau	4 21 59.5	19 32 06	60 ± 12	33 ± 6	0.25 ± 0.2	45	0.005
GK/GI Tau[e]	4 33 34.53/34.13	24 21 06/18	<2.0[f]/4.0 ± 0.8	1.0 ± 0.2/3.0 ± 0.6	1.0	40	0.001/0.003

NOTE.—Units of right ascension are hours, minutes, and seconds, and units of declination are degrees, arcminutes, and arcseconds.
[a] Measured continuum fluxes at 2.7 mm ($F_{2.7}$), and at 3.4 mm ($F_{3.4}$).
[b] We show the 1 σ error of our estimate of β, the power-law index of the dust emissivity. We assigned $\beta = 1$ to sources for which we do not have enough data to estimate its value (see text for details).
[c] Uncertainties in T_d are about 20%.
[d] Uncertainties in $M_{\rm cont}$ are about 30%.
[e] The dust continuum emission associated with GI Tau (a companion star to GK Tau) is also detected in the GK Tau field.
[f] Quoted value is 3 σ upper limit.

1997) at wavelengths greater than 60 μm using the estimated (or assumed) value of β. The measured fluxes at 2.7 and 3.4 mm, $F_{2.7}$ and $F_{3.4}$, respectively, and the estimated values of β, T_d, and $M_{\rm cont}$ are listed in Table 3.

4.2. ^{12}CO (1–0) *Outflows*

In Figure 1 we present integrated intensity maps of the ^{12}CO (1–0) emission associated with the observed sources. The central envelope velocity, $v_{\rm env}$, and the velocity ranges of integration are given in Tables 8 and 4, respectively. Blueshifted and redshifted components are detected for all sources; velocities deviate by at least 0.5 km s^{-1}, usually by more than 1 km s^{-1}, from $v_{\rm env}$. Since our interferometer observations filter out structures on scales greater than $\sim$30″, we are confident that the emission seen in Figure 1 traces molecular gas accelerated by the opposing outflow lobes close to the protostellar sources, and not ambient material. However, filtering of large-scale structures in our interferometer observations hampers our ability to *fully* recover the flux from the outflow gas present in the observed area.

The amount of filtered or missing flux in our OVRO data depends on the observed molecular outflow's structure; a smaller fraction of the total flux will be recovered from molecular outflows composed of smooth large-scale structures compared to the fraction of the total flux recovered from molecular outflows that are mainly made of compact structures. For three sources in our sample, we compared published ^{12}CO data from the Five College Radio Astronomy (FCRAO) 14 m telescope (Tafalla & Myers 1997; Lee et al. 2000; Arce & Goodman 2001) with our OVRO data averaged over a 46″ × 46″ area, the approximate beam size of the FCRAO ^{12}CO observations. We find that for L1228 our OVRO observations recover more than 60% of the flux at all outflow velocities and more than 90% of the flux at high outflow velocities. On the other hand, in HH 300 and RNO 91 we recover 15% and 20%, respectively, of the single-dish flux at outflow velocities. Evidently, the amount of missing flux is different for each molecular outflow. Here we do not attempt to correct for the missing flux in our OVRO data, as we lack the necessary single-dish data to do so for all sources. We stress that, regardless of how much flux is missing in each of the molecular outflow maps in our sample, our data are sensitive to the small-scale outflow structures—important for the study of the outflow-envelope interactions—and our maps reliably show the outflow morphology close to the source.

4.3. ^{13}CO (1–0) *Outflows*

In Figure 2, integrated intensity maps of the ^{13}CO emission toward our sample sources show gas that has been accelerated by the protostellar outflow and is slower and more dense than the ^{12}CO features. Like the ^{12}CO features, the morphology of the ^{13}CO blueshifted and redshifted outflow lobes varies substantially among sources. Nevertheless, with the exception of the red ^{13}CO lobe of GK/GI Tau, the locations and positional offsets of the ^{13}CO and ^{12}CO outflow lobes correspond well. In several sources the ^{13}CO outflow emission is concentrated at the outer edges of the ^{12}CO outflows and appears to delineate the dense outflow cavity walls. The blue lobes of L1228 and RNO 129 are particularly nice examples of this behavior, but it is also suggested for RNO 43. In other sources the ^{13}CO outflow concentrates at positions slightly offset from the protostar in the same direction as the corresponding ^{12}CO outflow lobes and generally has opening angles larger than that seen in ^{12}CO. This morphology is best illustrated by HH 114mms, HH 300, the red lobe of RNO 129, and the blue lobes of T Tau and IRAS 3282. Close to these sources, blueshifted and redshifted ^{13}CO traces dense gas that has been propelled by the protostellar outflow, as well as entrained dense gas in the outer outflow walls. On occasion, ^{13}CO is concentrated outside the limits of the ^{12}CO outflow, as in the red lobe of T Tau and the blue lobe of GK/GI Tau, perhaps due to the presence of a dense shell produced by the interaction between the protostellar outflow and the surrounding environment, similar to the larger scale morphology observed in other sources (e.g., Arce & Goodman 2002).

Similar to the ^{12}CO data, we expect that our ^{13}CO interferometer maps filter a substantial amount of flux (see § 4.2). For example, comparing single-dish (FCRAO) data of L1228 and HH 300 (Tafalla & Myers 1997; Arce & Goodman 2001) with our OVRO maps, we find that the interferometer ^{13}CO observations recover only 10% and 15%, respectively, of the flux in the outflow wings. This suggests that our OVRO observations filter most of the ^{13}CO (large scale) cloud emission and that the interferometer maps mainly show the (small scale) emission

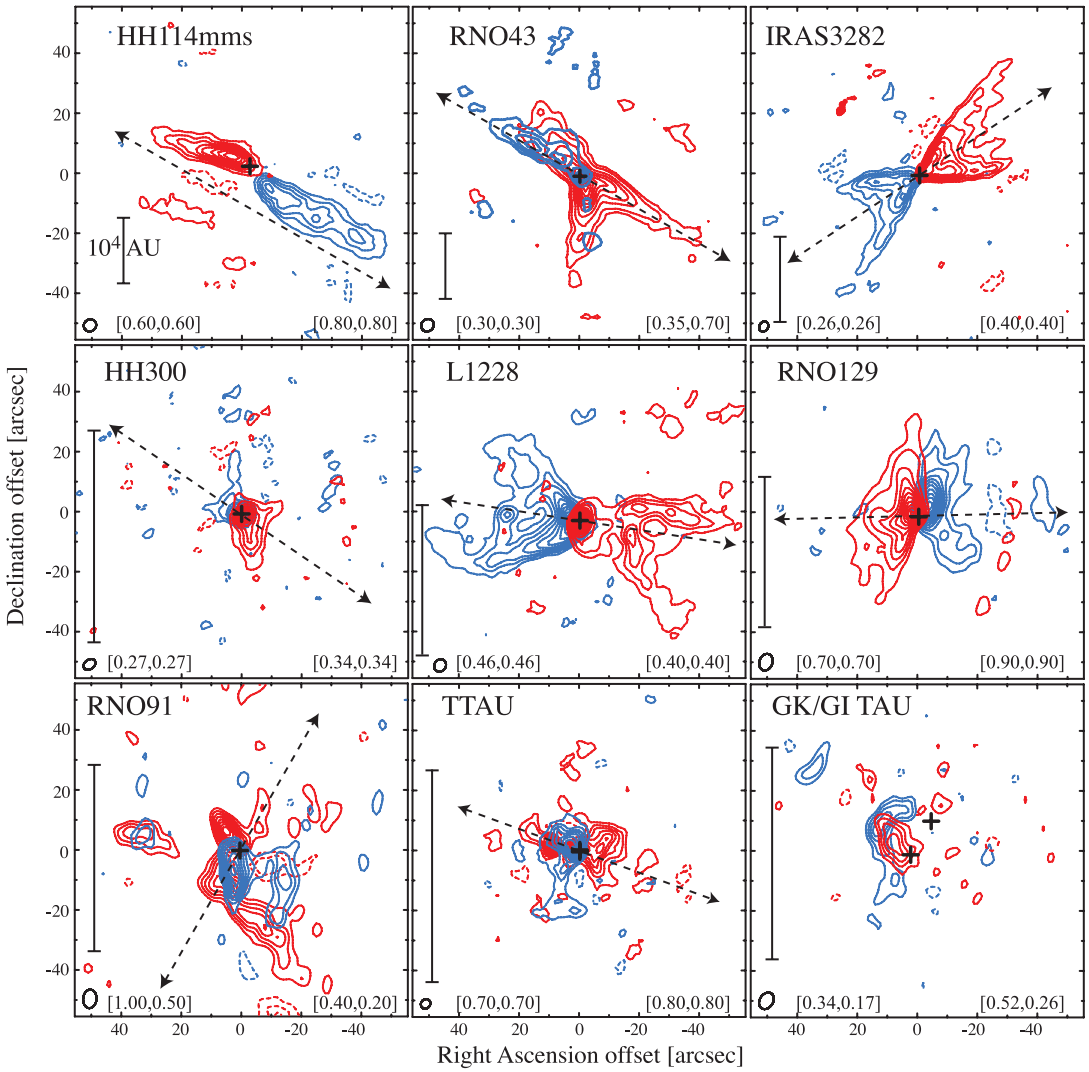

FIG. 1.—Gallery of ^{12}CO (1–0) outflows. Blue (red) contours show the blueshifted (redshifted) emission from the outflow lobes of the sources in our sample, integrated over the velocity ranges given in Table 4. *Top*, Class 0 objects; *middle*, Class I objects; *bottom*, Class II objects. A cross marks the position of the protostar given by the millimeter continuum emission peak. In each map, the synthesized beam is in the lower left corner. A scale equivalent to 10,000 AU at the assumed distance of each source is also given. The dashed line with arrowheads in each panel represents the presumed outflow axis. The values of the first contour and the subsequent contour steps for the blue (red) lobe of each outflow are given inside brackets in units of Jy km s^{-1}, at the lower left (right) corner of each panel.

TABLE 4

VELOCITY RANGES OF MOLECULAR OUTFLOW LOBES

SOURCE	^{12}CO OUTFLOW		^{13}CO OUTFLOW		HCO$^+$ OUTFLOW	
	Blue Lobe (km s^{-1})	Red Lobe (km s^{-1})	Blue Lobe (km s^{-1})	Red Lobe (km s^{-1})	Blue Lobe (km s^{-1})	Red Lobe (km s^{-1})
HH 114mms	[−10.05, −3.87]	[0.36, 8.16]	[−1.26, −1.08]	[0.10, 0.62]	...	[0.19, 1.23]
RNO 43	[6.02, 8.95]	[11.22, 16.10]	[10.11, 10.45][a]	[10.63, 11.14]	...	[10.76, 11.17]
IRAS 3282	[−2.75, 5.05]	[8.63, 16.10]	[5.98, 6.49]	[7.18, 7.52]	[4.28, 6.05]	[7.11, 9.52]
HH 300	[3.45, 6.05]	[7.03, 10.28]	[5.37, 6.02]	[7.04, 7.90]	[5.86, 6.07]	...
L1228	[−17.50, −9.05]	[−6.13, 2.00]	[−9.63, −8.60]	[−6.90, −6.40]	[−10.90, −9.02]	[−6.92, −5.02]
RNO 129	[−17.75, −10.93]	[−6.38, −2.14]	[−9.87, −8.17]	[−6.63, −5.79]	[−8.84, −8.21]	[−6.63, −5.90]
RNO 91	[−6.65, −0.80]	[1.15, 2.13]	[−0.70, −0.02]	[1.01, 1.34]	[−0.34, −0.10]	...
T Tau	[1.17, 6.70]	[9.30, 13.53]	[5.44, 7.14]	[8.52, 10.05]	[5.02, 7.19]	[8.81, 9.81]
GK/GI Tau	[4.95, 6.25]	[7.55, 9.50]	[5.87, 6.38]	[7.42, 7.92]	...	...

[a] Although the entire range of velocities is not blueshifted with respect to the RNO 43 ambient envelope velocity, 10.2 km s^{-1}, we are convinced the ^{13}CO structure at these velocities traces the outflow cavity walls of the RNO 43 blueshifted outflow (see Paper II).

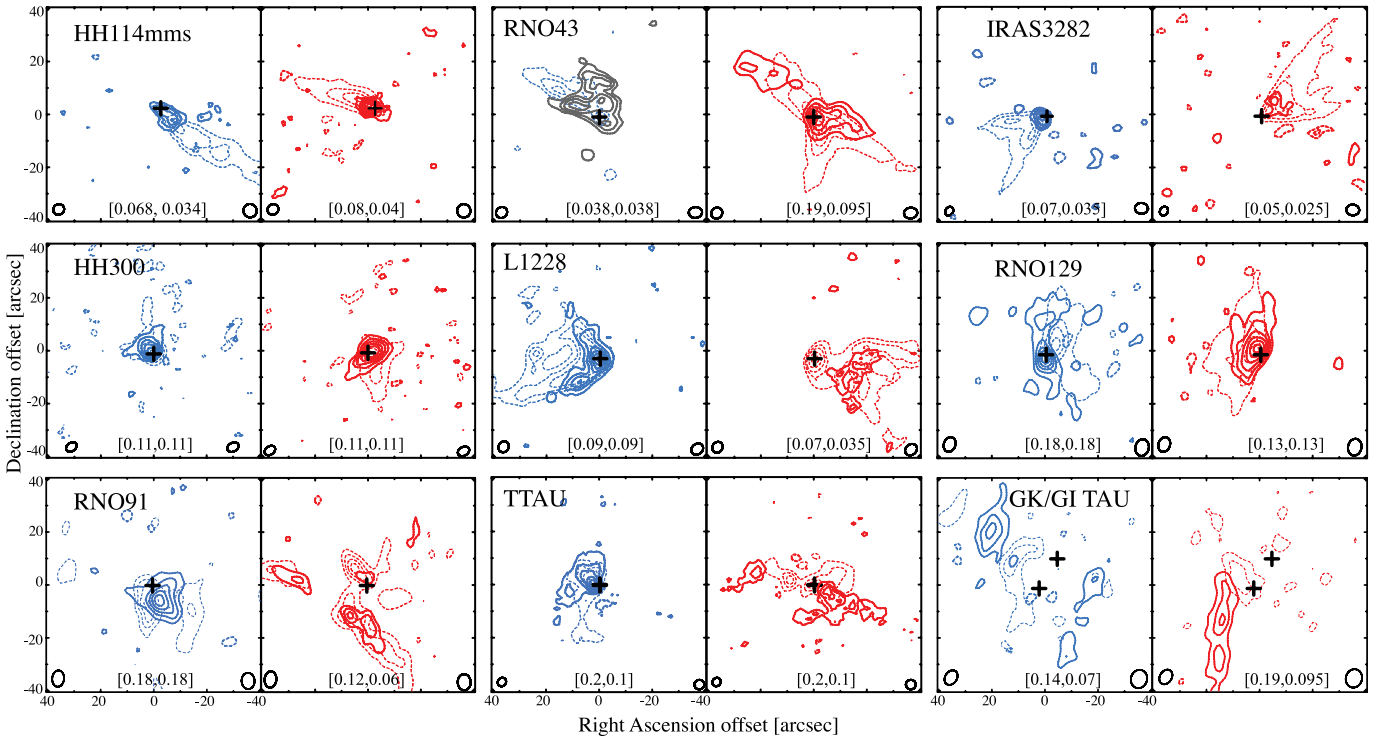

FIG. 2.—Gallery of ^{13}CO (1–0) outflows. Solid blue (red) contours show the blueshifted (redshifted) integrated intensity. The dashed contours show the ^{12}CO outflows (shown in Fig. 1). The velocity range of integration for each ^{13}CO outflow lobe is given in Table 4. The cross symbol indicates the position of the protostar, given by the millimeter continuum emission peak. The synthesized beam of the ^{13}CO (^{12}CO) map is shown on the lower right (left) corner of each panel. The scale in each panel shows the equivalent of 5000 AU at the assumed source distance. The values of the first contour and the subsequent contour steps for each outflow lobe are given inside brackets in units of Jy km s^{-1}. In the case of RNO 43, the "blueshifted" lobe is shown in gray, as the gas velocities are very close to the ambient envelope velocity. The RNO 43 outflow axis is very close to the plane of the sky; thus this ^{13}CO structure most likely traces the walls of the outflow cavity of the blueshifted outflow lobe, albeit its velocities (see Paper II).

associated with the envelope and the regions where it is being impacted by the underlying protostellar wind.

4.4. *Molecular Outflow Parameters*

The ^{12}CO line is expected to be optically thick at velocities close to the ambient envelope velocity and optically thin at high outflow velocities. Thus, we use ^{12}CO emission to estimate the mass of the low-density, high-velocity component of the molecular outflow and ^{13}CO emission to account for higher density, lower velocity material (see Papers I and II for more details). At outflow velocities where the ^{12}CO line is extremely optically thick and there is detectable resolved ^{13}CO outflow emission, we derive the outflow mass from the ^{13}CO emission, as it is expected to be optically thin at these relatively high velocities far from the line core. Outside the velocity regimes where we use ^{13}CO, we estimate the outflow mass from the ^{12}CO emission.

We estimate the outflow mass, $M_{\rm out}$, from the ^{12}CO and ^{13}CO data, assuming LTE and a gas temperature of 25 K. We adopt $[{\rm H_2}]/[^{13}{\rm CO}] = 7 \times 10^5$ (Frerking et al. 1982) and $[^{13}{\rm CO}]/[^{12}{\rm CO}] = 62$ (Langer & Penzias 1993). We obtain the outflow momentum,

TABLE 5
MOLECULAR OUTFLOW PARAMETERS I

Source	Outflow Axis P.A. (deg E of N)	Opening Angle[a] (deg)	$M_{\rm out}$ ($10^{-3}\ M_\odot$)	$P_{\rm out}$[b] ($10^{-3}\ M_\odot$ km s^{-1})	$E_{\rm out}$[b] (10^{40} ergs)
HH 114mms	60	25	30	91	484
RNO 43	60	45	150	119	142
IRAS 3282	125	50	15	44	195
HH 300	59	80	8	6	2
L1228	79	95	13	26	92
RNO 129	95	125	24	36	94
RNO 91	155	160	11	11	20
T Tau	75	100	21	25	37
GK/GI Tau	[c]	...	6	4	4

[a] The outflow opening angle was estimated the following way: in HH 114mms we used the lowest velocity blueshifted ^{12}CO; in RNO 43 and L1228 we used the blushifted ^{13}CO outflow lobe shown in Fig. 2; in IRAS 3282, HH 300, RNO 129, and T Tau we used both lobes of the ^{12}CO outflow shown in Fig. 1; in RNO 91 we used the opening angle estimate from Lee & Ho (2005); in GK/GI Tau we were unable to determine the opening angle from our maps.
[b] Estimated value not corrected for outflow inclination with respect to the plane of the sky.
[c] Unknown outflow axis due to uncertainty as to which source powers the observed outflow.

TABLE 6
MOLECULAR OUTFLOW PARAMETERS II

Source	$\dot{M}_{\rm out}$[a] ($10^{-7}\ M_\odot\ {\rm yr}^{-1}$)	$F_{\rm CO}$[a] ($10^{-6}\ M_\odot\ {\rm km\ s}^{-1}\ {\rm yr}^{-1}$)	$\dot{M}_{\rm den}$[a] ($10^{-7}\ M_\odot\ {\rm yr}^{-1}$)
HH 114mms.....	41	16	11
RNO 43.....	73	9	51
IRAS 3282.....	31	11	4
HH 300	18	1	16
L1228.....	29	15	13
RNO 129.....	56	14	37
RNO 91.....	16	3	11
T Tau.....	47	8	36
GK/GI Tau.....	2	0.2	2

[a] Estimated value not corrected for outflow inclination with respect to the plane of the sky.

$P_{\rm out} = \Sigma_v M_{\rm out}(v)v$, and kinetic energy, $E_{\rm out} = (1/2)\Sigma_v M_{\rm out}(v)v^2$, for each source and list their values in Table 5. In addition, we calculate the mass outflow rate, $\dot{M}_{\rm out} = \Sigma_v M_{\rm out}(v)/\tau$, and the flow momentum rate, $F_{\rm CO} = \Sigma_v M_{\rm out}(v)v/\tau$ (see Table 6), where $\tau = v/r$ is the dynamic timescale of the outflow gas, v is the outflow velocity, and r is the distance from the source to the outflow gas. In Table 6 we also show the dense gas mass outflow rate, $\dot{M}_{\rm den} = \Sigma_v M_{\rm den}(v)/\tau$, where $M_{\rm den}$ is the outflow mass traced solely by the ^{13}CO emission.

For all mass-related outflow parameters listed in Tables 5 and 6 (except for $\dot{M}_{\rm den}$, where we only use the ^{13}CO emission) the final estimate is the summation of the estimates from both the ^{12}CO and ^{13}CO emission. These values should be treated as lower limits, since no correction for missing flux, opacity, or outflow inclination angle have been applied. Care should also be taken when comparing $M_{\rm out}$, $P_{\rm out}$, and $E_{\rm out}$ for the individual outflows, since the areas observed are in effect the linear sizes of the interferometer primary beam and differ according to source distance. Nevertheless, to the first order $\dot{M}_{\rm out}$, $F_{\rm CO}$, and $\dot{M}_{\rm den}$ do not depend on the observed area (Henning & Launhardt 1998).

4.5. HCO^+ *Outflows*

In Figure 3 the HCO^+ emission at $|v_{\rm env}| > 0.5$ km s^{-1} appears to coincide with the molecular outflow lobes. Indeed, outflowing HCO^+ (1–0) is observed in all sources except GK/GI Tau, although not all show both blueshifted and redshifted emission.

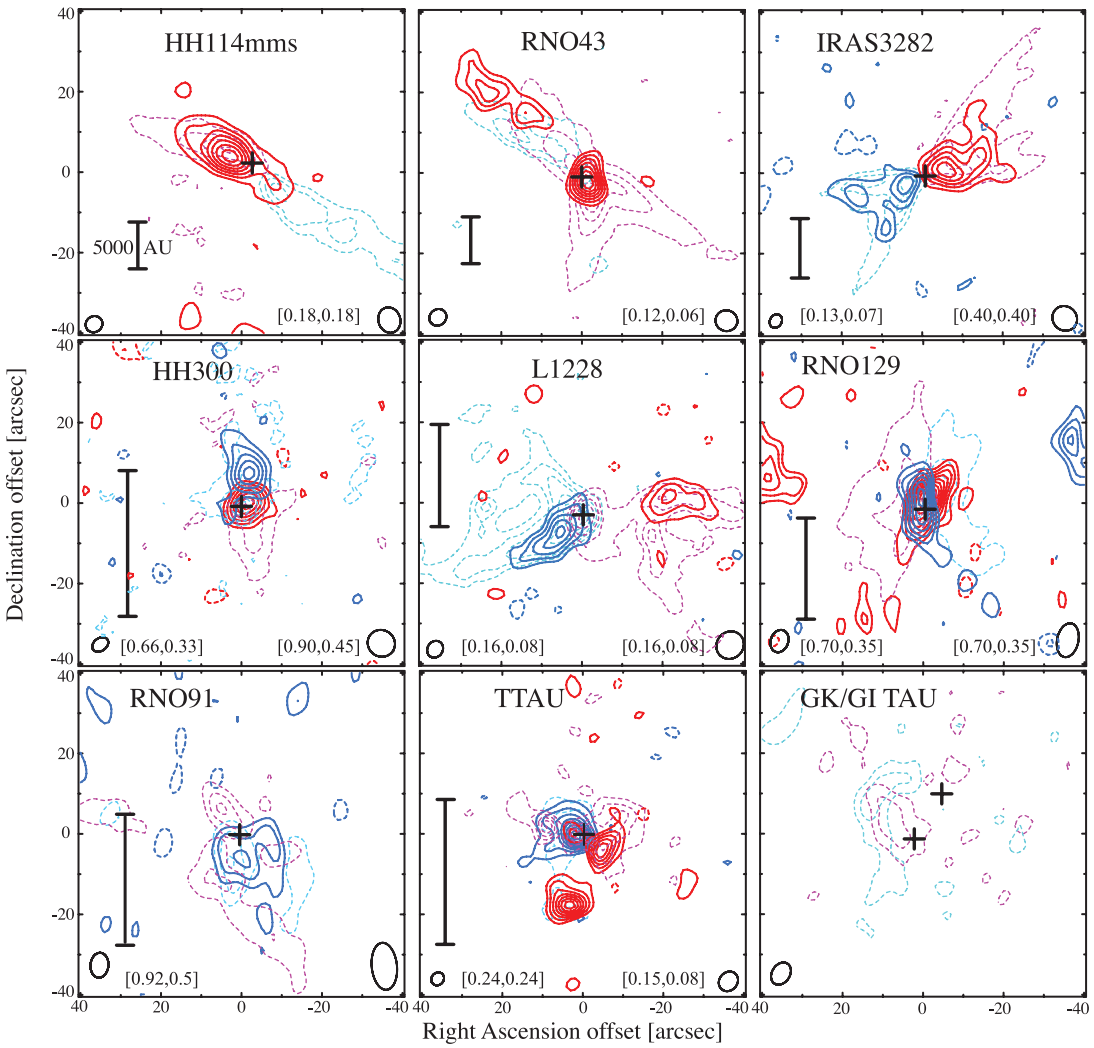

FIG. 3.—Gallery of HCO^+ (1–0) outflows. Solid blue (red) contours represent integrated intensity of blueshifted (redshifted) HCO^+ emission. Dashed contours represent ^{12}CO molecular outflow. The synthesized beam of the HCO^+ (^{12}CO) map is shown on the lower right (left) corner of each panel. The values of the first contour and the subsequent contour steps for the blue (red) lobe of each outflow are given inside brackets in units of Jy km s^{-1}, at the lower left (right) corner of each panel.

TABLE 7
HCO$^+$ Abundance in Outflows

Source	$[HCO^+]/[H_2]$ Blue Lobe (10^{-9})	$[HCO^+]/[H_2]$ Red Lobe (10^{-9})
HH 114mms	...	>20
RNO 43	...	>2
IRAS 3282	>2	>60
HH 300	5	1
L1228	>7	>4
RNO 129	0.5	0.6
RNO 91	1	...
T Tau	4	3
GK/GI Tau	...	...

In general, this HCO$^+$ is confined to the outflow cavity walls. In this respect it echoes the behavior of ^{13}CO, but, as can be seen in Table 4, the velocity range exceeds that of the ^{13}CO outflow emission in most sources, and, as can be seen in Figure 3, in some sources the HCO$^+$ outflow emission does not trace the full extent of the outflow cavity walls. As in the ^{13}CO data, we expect that our interferometer observations have filtered much of the extended emission and that the HCO$^+$ outflow maps show the compact structures in the envelope, where the gas has been influenced by the prostellar outflow.

The HCO$^+$ abundance in the outflow, X_{HCO^+}, should indicate whether outflow-triggered chemical processes have affected the surrounding gas. The ^{13}CO outflow emission along the outflow cavity walls and offset from the source position is probably optically thin, since there is no C^{18}O at these velocities and positions. Thus, it provides a reliable estimate of the molecular hydrogen column density, N_{H_2}, using the same assumptions as in § 4.4. The HCO$^+$ column density, N_{HCO^+}, can be obtained assuming the emission is optically thin and leads to the outflow HCO$^+$ abundance using $X_{HCO^+} = N_{HCO^+}/N_{H_2}$, where N_{H_2} (from the ^{13}CO data) and N_{HCO^+} are obtained over the exact same area and velocity range. The *u-v* coverage and beam sizes of our ^{13}CO and HCO$^+$ data are very similar. Thus, these maps are sensitive to similar structures in the emission and may be used to obtain a reliable estimate of the HCO$^+$ abundance in the outflow and outflow-envelope interface, close to the protostar. Given that an estimate of X_{HCO^+} can only be obtained in regions where the

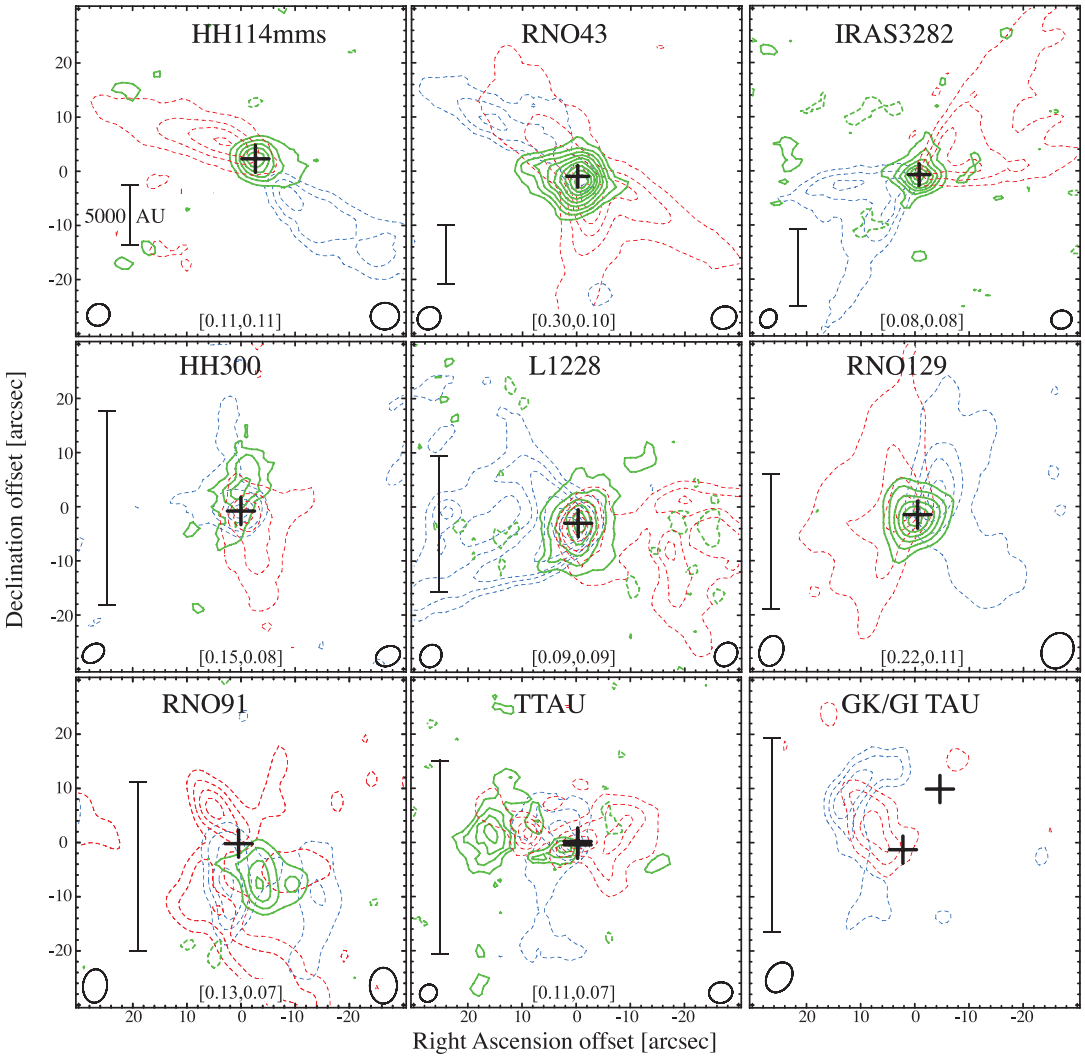

Fig. 4.—C^{18}O integrated intensity (*solid green lines*) contour maps superimposed on ^{12}CO outflows (*dashed contour lines*). The velocity range of integration for each source is given in Table 8. The synthesized beam of the C^{18}O (^{12}CO) map is shown on the lower right (left) corner of each panel. The scale in each panel shows the equivalent of 5000 AU at the assumed source distance. The values of the first contour and the subsequent contour steps are given in brackets at the bottom of each panel.

TABLE 8
$C^{18}O$ (1–0) Envelope Parameters

Source	Velocity Range[a] (km s^{-1})	Size[b] (AU)	P.A.[c] (deg E of N)	M_{env} ($M_\odot$)	v_{env} (km s^{-1})	Reference[d]
HH 114mms	[−1.09, 0.28]	2700 × 1400	69	0.13	−0.46	1
RNO 43	[9.26, 11.48]	6200 × 5000	75	0.87	10.20	1
IRAS 3282	[6.32, 7.68]	1900 × 1600	113	0.08	6.96	1
HH 300	[5.84, 7.21]	3700 × 1300	161	0.03	6.50	2
L1228	[−8.77, −7.41]	2400 × 1500	161	0.05	−8.00	1
RNO 129	[−8.35, −6.29]	2000 × 1500	149	0.04	−7.60	1
RNO 91	[−0.35, 0.33]	...	...	0.01	0.57	1
T Tau	[7.15, 8.34]	...	...	0.02	7.90	3
GK/GI Tau	...	...	...	<0.001[e]	6.90	4

[a] Lower and upper limits of velocity range for which $C^{18}O$ emission was detected above the 3 σ level.
[b] FWHM size of $C^{18}O$ envelope from a Gaussian fit to the integrated intensity map, deconvolved by the beam.
[c] Deconvolved position angle of the Gaussian fitted to the $C^{18}O$ integrated intensity emission.
[d] References for estimate of v_{env}: (1) our observations; (2) Fuller & Ladd 2002; (3) average of values used by Momose et al. 1996 and van Langevelde et al. 1994a; (4) peak velocity at position of GK Tau from Mizuno et al. 1995.
[e] Quoted value is 3 σ upper limit.

HCO^+ and ^{13}CO emission coincide in position and velocity and that in some sources the HCO^+ emission arises from positions and velocities where ^{13}CO is not detected, we can obtain only a lower limit to X_{HCO^+} for most of our sources (see Table 7).

4.6. $C^{18}O$ (1–0) *Envelopes*

Integrated intensity maps of the $C^{18}O$ emission associated with our sample are shown in Figure 4. For the Class 0 and Class I sources, $C^{18}O$ emission usually coincides with continuum peak positions. Elliptical Gaussian fits indicate geometric mean sizes (after beam deconvolution) of about 2000 AU (FWHM), independent of evolutionary stage. An exception is RNO 43, for which the $C^{18}O$ emission region size is about 5600 AU (FWHM; see Table 8). The compact morphology and spatial coincidence with the dust continuum peaks strongly suggest that the $C^{18}O$ emission traces the dense circumstellar envelope gas in these Class 0 and I sources. By contrast, $C^{18}O$ emission is significantly offset from the positions of our Class II sources and may trace the remnants of the high-density ($n \gtrsim 10^4$ cm^{-3}) circumstellar envelope gas that has been mostly cleared by the protostellar outflow (see § 5.4).

Comparing the total $C^{18}O$ flux obtained from single-dish (FCRAO) data of two sources (HH 300: Arce & Goodman 2001; IRAS 3282: Hatchell et al. 2005) with the flux recovered by our interferometer data (smoothed to the same beam size), we estimate that the OVRO observations trace 1%–4% of the total flux traced by the FCRAO observations. In addition, the velocity distribution of the emission in the single-dish data is very different from that of our OVRO data. These properties support the idea that the two sets of data trace entirely different structures: the $C^{18}O$ emission detected in our OVRO data arises from the compact structure of dense gas surrounding the protostar (i.e., the circumstellar envelope or its remnants), while the single-dish $C^{18}O$ observations trace the surrounding (large scale) cloud. Thus, our $C^{18}O$ OVRO data can be used to obtain an estimate of the circumstellar envelope mass (e.g., Hogerheijde et al. 1998).

We estimate the masses of the dense circumstellar envelope, M_{env}, assuming optical thin $C^{18}O$ emission, LTE, and an abundance ratio of $[C^{18}O]/[H_2] = 1.7 \times 10^{-7}$ (Frerking et al. 1982). We adopt an excitation temperature, T_{ex}, of 25 K, since T_{ex} probably lies between 10 and 40 K; the lower limit is given by the "typical" temperature of an isolated dense core (Jijina et al. 1999), while the upper is the "typical" T_d of our sources. Envelope masses and other properties are listed in Table 8.

5. DISCUSSION

5.1. *Outflow Opening Angle*

The CO outflows displayed in Figure 1 have very different morphologies, due in part to their various surrounding environments. Nevertheless, there are significant trends. The molecular outflows from the youngest protostellar sources (Class 0) tend to be highly collimated with either jetlike morphologies or cone-shaped lobes with relatively small opening angles of less than 55°. As discussed in Paper II, the morphology and kinematics of one of these, the RNO 43 outflow, strongly suggest that it results from the entrainment of ambient gas by an underlying collimated jet. Likewise, the significant collimation of the HH 114mms molecular outflow, as well as the fact that the outflow velocity increases with distance from the source, indicates that it is also driven by a jet or by a very collimated, momentum-conserving wind (e.g., Lee et al. 2001). The cone-shaped morphology of the IRAS 3282 outflow resembles that observed in other Class 0 outflows, such as L1448 (Bachiller et al. 1995), L1157 (Gueth et al. 1996), and HH 211 (Gueth & Guilloteau 1999). These cone-shaped morphologies have been successfully fitted with jet bow shock entrainment models (e.g., Raga & Cabrit 1993). By analogy, we propose that the outflow lobes in IRAS 3282 represent the walls of a cavity produced by a jet bow shock. The limited velocity range of our ^{12}CO observations (see Table 4) precludes our detecting the high-velocity collimated component of IRAS 3282 that has been observed in single-dish maps at outflow velocities of ~50 km s^{-1} by Bachiller et al. (1991).

The sightly more evolved (Class I) sources in our sample have ^{12}CO outflows with lobe opening angles of more than 75°. This wide-angle morphology is also seen in ^{13}CO (Fig. 2) with opening angles for L1228, HH 300, and RNO 129, which are as wide as, if not wider than, their ^{12}CO counterparts. Near-infrared and optical scattered light nebulae associated with these sources (Bally et al. 1995; Reipurth et al. 2000; Movsessian & Magakian 2004) display morphologies that are very similar to those of the molecular outflow lobes, consistent with the high-velocity ^{13}CO emission tracing the walls of cavities produced by the protostellar outflow.

By contrast, outflows from the most evolved young stars in our sample, the Class II sources, have no definite shape or structure.

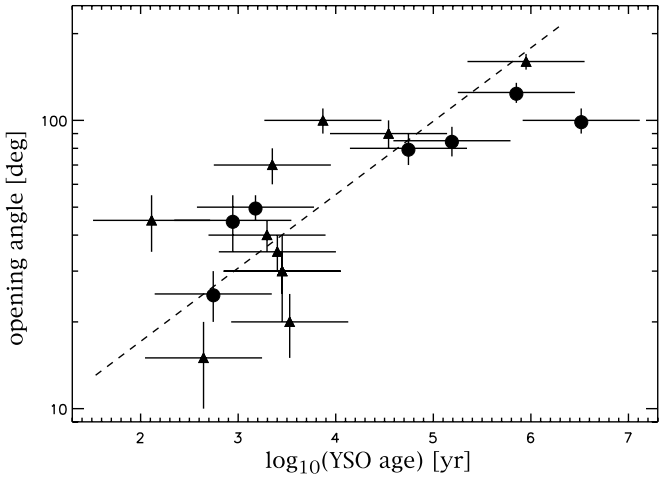

FIG. 5.—Outflow opening angle as a function of source age. The source age was obtained using the T_{bol}-age relation from Ladd et al. (1998). Circles show sources in our sample for which we were able to measure an outflow opening angle (see Tables 1 and 5), and the triangles show sources from the literature (see Table 9). The dashed line represents the fit to all the data shown in the figure. The errors in the opening angle come from the uncertainty of the angle measurement, while the errors in the age come mainly from the T_{bol}-age relation.

TABLE 9

OUTFLOW OPENING ANGLE FROM LITERATURE

Source	T_{bol} (K)	Reference[a]	Opening Angle[b] (deg)	Reference[c]
IRAM 04191	18	1	45	1
HH 211	30	1	15	2
L1448	56	1	40	3
L1527	59	1	70	4
L1157	62	1	35	5
HH 114/115	65	2, 3, 4	30	1
RNO 40	65	2, 3, 4	30	6
HH 111	70	2, 3, 4	20	6
L1551-IRS 5	97	1	100	7
B5-IRS 1	185	4, 5, 6	90	8

[a] T_{bol} obtained from estimates shown in (1) Buckle & Fuller 2002, or calculated from SED using data from the literature: (2) Reipurth et al. 1993; (3) Dent et al. 1998; (4) IRAS Catalog of Point Sources; (5) 2MASS All-Sky Catalog of Point Sources; (6) Langer et al. 1996.

[b] Uncertainty in opening angle estimate is about 5°–10°.

[c] Reference for opening angle estimate: (1) Lee et al. 2002; (2) Gueth & Guilloteau 1999; (3) Bachiller et al. 1995; (4) Ohashi et al. 1997; (5) Gueth et al. 1996; (6) Lee et al. 2000; (7) Ohashi et al. 1996; (8) Langer et al. 1996.

Blueshifted and redshifted gas within about 6000 AU of RNO 91, T Tau, and GK/GI Tau shows neither the collimated appearance of the Class 0 outflows nor the wide-angle morphology characteristic of the Class I sources. Class II sources are generally found in regions of low ambient density (Myers et al. 1987), and the clumpy structures seen in Figure 1 may arise only in the (limited) regions where molecular gas around the nascent star has not yet been cleared by the protostellar outflow. RNO 91 is a case in point. A large-scale mosaic of ^{12}CO interferometer observations, covering an area about 5×10^4 by 10^5 AU, demonstrates that the outflow has produced a 3×10^4 AU wide cavity, with an opening angle of 160° (Lee et al. 2002; Lee & Ho 2005). Thus, our observations of the RNO 91 source, with a primary beam of $\sim 5 \times 10^3$ AU, cannot fully map the cavity walls seen in the maps of Lee et al. (2002); instead, we can expect to detect only remnant molecular material that has not been swept up out of the field of view of our maps. A similar scenario applies for T Tau (Momose et al. 1996) and perhaps for GK/GI Tau.

In Figure 5 we plot the opening angle, θ, of each of our observed outflows as a function of the source age, together with published data of other spatially resolved molecular outflows from low-mass YSOs within 500 pc of the Sun, where the outflow opening angle near the source could easily be measured (see Table 9). In cases where the value of θ depends on velocity, we have adopted the largest opening angle. It is immediately clear that there is a tendency for the outflow opening angle to increase with the evolutionary stage of the outflow source. A fit to our data alone yields $\log(\theta/\mathrm{deg}) = (1.1 \pm 0.2) + (0.16 \pm 0.4) \log(t/\mathrm{yr})$, quite consistent with the fit to the combined data, $\log(\theta/\mathrm{deg}) = (0.7 \pm 0.2) + (0.26 \pm 0.4) \log(t/\mathrm{yr})$.

Although an increase of outflow opening angle with age has been inferred by other authors (e.g., Richer et al. 2000), it has never been clear whether the trend was a real effect or due to the varying beam sizes in independent studies of individual sources observed at lower resolution with single telescopes. Indeed, high-resolution observations indicated that the opening angle of the B5-IRS1 outflow is widening at about $0\overset{\circ}{.}006\ \mathrm{yr}^{-1}$ (Velusamy & Langer 1998), but there was no suggesting evidence to confirm that this was a general trend. It is true that interferometer mapping of a sample of molecular outflows from sources at different evolutionary stages concluded that outflow *widths* increase with age (Lee et al. 2002). However, we argue that the outflow opening angle is a better probe of the outflow's impact on the envelope, since it is measured close to the protostar, where the outflow-envelope interactions are strongest. Outflow width, by contrast, may be measured anywhere along the outflow length, including regions far away from the circumstellar envelope. Our results demonstrate unambiguously that outflow opening angles increase with source age, implying a progressively stronger outflow-envelope interaction.

5.1.1. *Why Should We Expect Outflow Widening?*

There is as yet no generally accepted explanation for the observed outflow widening. It has been proposed that jet axis wandering (precession) could produce wider cavities as the protostar evolves (Masson & Chernin 1993). However, although ample evidence for jet wandering exists (e.g., Reipurth et al. 1997; Terquem et al. 1999), in most sources the opening angle of the precession cone is smaller than the observed wide-angle outflow cavity (e.g., Yu et al. 1999; Reipurth et al. 2000; Paper I). Our study of the L1228 outflow also shows that the detailed morphology of the wide-angle cavities is incompatible with their being produced by jet entrainment (Paper I). An attractive alternative is an underlying stellar wind with both a collimated and a wide-angle component (e.g., Kwan & Tademaru 1995; Königl & Pudritz 2000; Shu et al. 2000; Matt et al. 2003), where the observed molecular outflow is predominantly driven by one of the two components, depending on the age of the protostar. The *X*-wind model of Shang et al. (1998), for example, predicts a stellar wind with a high density along the axis (very similar to a jet), but decreasing density at increasing angles from the axis. It is conceivable that at very early ages only the dense collimated part of the wind can break out of the surrounding dense (infalling) envelope (e.g., Wilkin & Stahler 2003), thereby producing the jetlike outflows observed in Class 0 sources. As the envelope loses mass, through infall onto the star-disk system *and* outflow entrainment along the axis (see § 5.4), the less dense and wider wind component will break through, entraining the gas unaffected by the collimated component. At this stage there

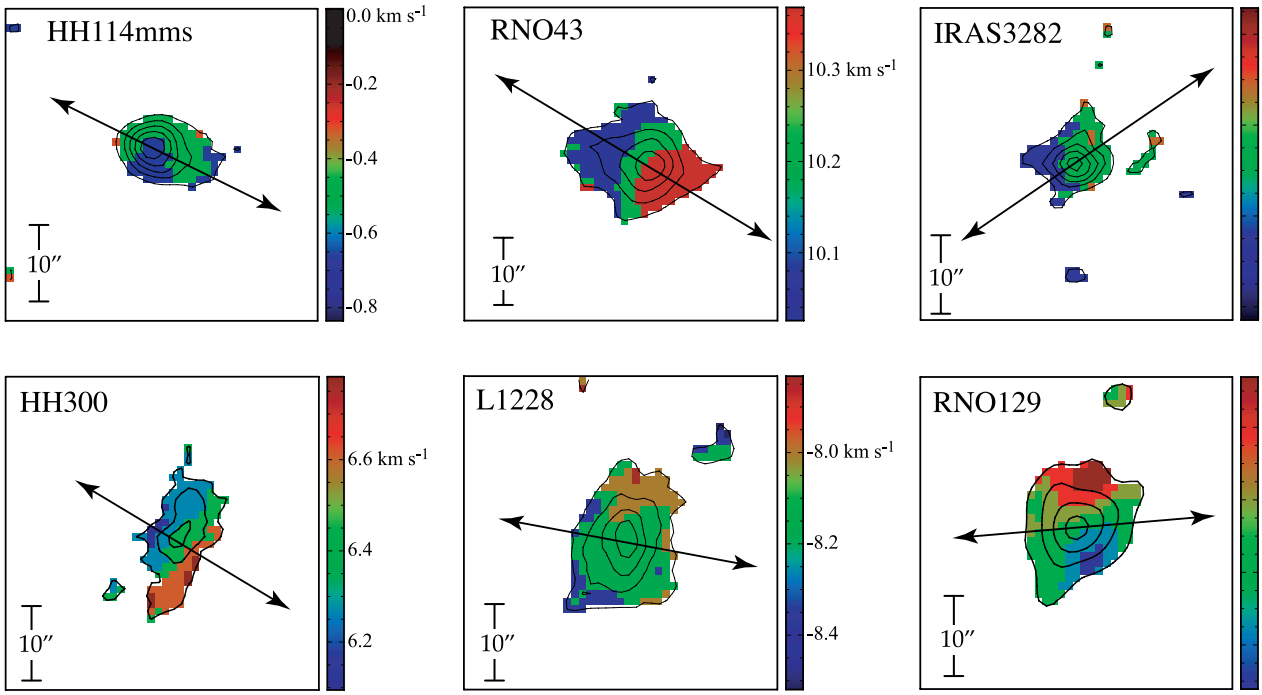

FIG. 6.—First-moment maps of the $C^{18}O$ (1–0) line from our Class 0 (*top row*) and Class I (*bottom row*) sources. The first moment between two velocities, v_1 and v_2, is defined as $\int_{v_1}^{v_2} T_B v\, dv / \int_{v_1}^{v_2} T_B\, dv$, where T_B is the brightness temperature. The color bar to the right of each panel shows the color that represents the velocity in each map. Contours represent integrated intensity levels similar to those of Fig. 4. The arrow shows the ^{12}CO outflow axis from Fig. 1.

will be almost no gas along the outflow axis, and the gas entrained by the wide-angle component of the wind will be the dominant structure in the molecular outflow, as seen in Class I sources. A decrease in infall as the protostar evolves (e.g., Henriksen et al. 1997) could also allow the wind to carve out wide-angle cavities (see Delamarter et al. 2000).

5.2. *Evolution in the Envelope's Morphology and Kinematics*

There also appears to be a change in the $C^{18}O$ morphology as the outflow source evolves. From Tables 5 and 8 it is clear that for Class 0 sources the $C^{18}O$ is usually elongated along an axis within 15° of that of the outflow. In Figure 6, two Class 0 sources, RNO 43 and IRAS 3282, display velocity gradients along the (elongated) major axis of the envelopes, in the same sense as the outflow. There is no clear velocity gradient in the $C^{18}O$ envelope of HH 114mms, although the gas at the extreme southwest edge of the envelope is blueshifted—similar to the CO outflow. Based on our detailed analysis of $C^{18}O$ emission in RNO 43 (Paper II), we suggest that the outflow is responsible for the velocity field and morphology of the high-density envelope around at least two Class 0 sources in our sample.

On the other hand, Figure 6 and Tables 5 and 8 indicate that the $C^{18}O$ envelopes around the Class I sources tend to be elongated perpendicular to the outflow axis, and there is no obviously shared velocity distribution. For both RNO 129 and L1228 the $C^{18}O$ velocity gradient is aligned with the major axis of the envelope and perpendicular to the outflow axis, consistent with rotation. In HH 300, the envelope velocity gradient is along the *minor* axis, parallel to the outflow axis, suggesting a flattened infalling envelope, where infall motions produce blueshifted and redshifted emission in the far and near sides of the structure, respectively (as seen in other sources; e.g., Torrelles et al. 1995; Ohashi et al. 1997; Momose et al. 1998). Contrary to what is observed in the Class 0 sources shown here and in the literature, where the outflow is clearly impacting the dense circumstellar gas (i.e., Gueth et al. 1997; Wiseman et al. 2001; Beltrán et al. 2004), the $C^{18}O$ emission in HH 300 is elongated perpendicular to the outflow at all velocities and does not show any protrusion along the outflow axis. We are, therefore, certain that the HH 300 velocity distribution is mainly (if not all) due to infall.

For Class II sources, either no $C^{18}O$ emission is detected, or the emission is offset in both position and velocity from the protostar. Specifically, the $C^{18}O$ emission associated with RNO 91 is about 8″ (1300 AU) southwest of the continuum peak and is seen only at velocities that are blueshifted with respect to that of the ambient envelope velocity. Similarly, the $C^{18}O$ emission associated with T Tau is concentrated 15″ (2100 AU) east of the young star, and most of the emission emerges at velocities blueshifted by 0.2–0.5 km s^{-1} with respect to v_{env}. In both cases the $C^{18}O$ emission is concentrated toward the edge of the outflowing ^{12}CO structure seen in Figure 1. No $C^{18}O$ emission within our sensitivity levels was detected from GK/GI Tau. As we describe in § 5.4, we interpret these changes in the $C^{18}O$ envelope properties between Class 0 and Class II sources as a real evolutionary progression due to the protostellar outflow's effect on the dense circumstellar gas.

5.3. *Envelope Mass Evolution*

In Figure 7 we plot our estimate of the envelope mass derived from the $C^{18}O$ emission, M_{env}, as a function of source age, determined from the T_{bol}-age relationship of Ladd et al. (1998). Although the correlation is not very tight, M_{env} is certainly greater for younger protostars than for more evolved YSOs. We would not expect any relation between T_{bol} and M_{env} a priori, since T_{bol} is obtained from the SED and thus is an indirect measure of the dust content close to the protostar rather than the gas.

A linear fit to the log (M_{env})-log (age) plot results in

$$\log (M_{env}/M_\odot) = (0.87 \pm 0.5) - (0.45 \pm 0.09) \log (t/\mathrm{yr}), \quad (1)$$

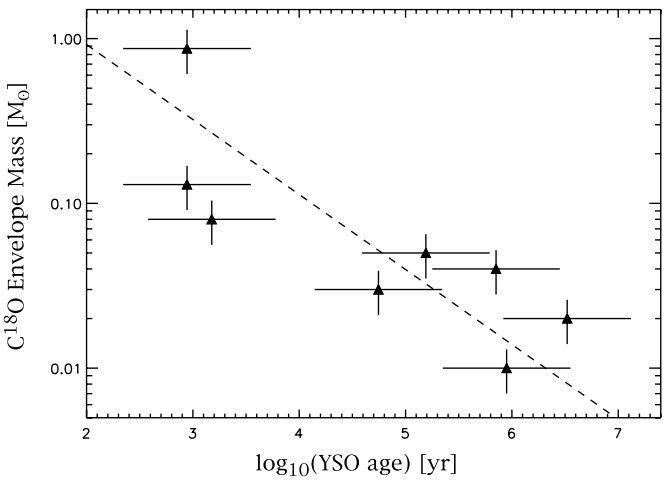

FIG. 7.—Envelope mass as a function of protostar age. The envelope mass was obtained from the $C^{18}O$ emission (see Table 8). The protostar age was obtained using the T_{bol}-age relation from Ladd et al. (1998). The dashed line represents the fit to all the data shown in the figure. The error bars in the envelope mass reflect the 30% calibration uncertainty in the data, while the errors in the age come mainly from the T_{bol}-age relation.

with a correlation coefficient of 0.8. Taking the derivative leads to a rough estimate of the envelope mass-loss rate, $\dot{M}_{env}$, from

$$\dot{M}_{env} \sim -3t^{-1.45}. \quad (2)$$

Evidently, $\dot{M}_{env}$ decreases rapidly with time from $\dot{M}_{env} \sim 10^{-4}\ M_\odot$ yr^{-1} for sources with age 10^3 yr to 5×10^{-6} and $2 \times 10^{-7}\ M_\odot$ yr^{-1} for ages of 10^4, and 10^5 yr, respectively. This is consistent with the core mass-loss rate found by Ladd et al. (1998), $\dot{M} \propto t^{-1.52\pm0.55}$, from lower resolution $C^{18}O$ (1–0) observations of a sample of Taurus cores harboring deeply embedded YSOs.

Does the protostellar outflow play a role in the mass-loss of the circumstellar envelope? As discussed in § 4.3 (and in Papers I and II in more detail), high-velocity ^{13}CO traces dense envelope gas that has been entrained by the protostellar wind and thus provides an estimate of the outflow rate of the relatively dense gas that could escape the envelope's gravitational potential. The dense gas mass outflow rate, $\dot{M}_{den}$, shown in Table 6, is approximately constant across our sample, mostly ranging from only 1 to about $5 \times 10^{-6}\ M_\odot$ yr^{-1}, independent of the source's age. Only two sources, IRAS 3282 and GK/GI Tau, deviate, with $\dot{M}_{den}$ values of $\sim$4 and $2 \times 10^{-7}\ M_\odot$ yr^{-1}, respectively. The median (and average) value of $\dot{M}_{den}$ from our whole sample is between 1 and $2 \times 10^{-6}\ M_\odot$ yr^{-1}. This is very close to the value of the envelope mass-loss rate for late Class 0/early Class I sources with ages of about 10^4 yr, $\dot{M}_{env} \sim 5 \times 10^{-6}\ M_\odot$ yr^{-1} (see eq. [2]). It is therefore conceivable that a fraction of the mass-loss in the envelope is due to the outflow entrainment of dense envelope gas. In Class I (and older) sources with ages $>10^5$ yr the envelope mass-loss rate is even less, $\dot{M}_{env} < 2 \times 10^{-7}\ M_\odot$ yr^{-1}, about a factor of 10 smaller than the average $\dot{M}_{den}$ in our sample. Therefore, in Class I (and older) sources, even if only 10%–20% of the dense mass entrained by the outflow eventually escapes from the envelope's gravitational potential, the outflow-envelope interaction can contribute significantly to the envelope's mass loss.

We note that in sources younger than $\sim 10^3$ yr the outflow may be responsible for only a small fraction of the total mass loss in the envelope, since the estimated dense gas outflow mass rate is less than 10% of the estimated envelope mass-loss rate. This accords well with theoretical and observational work suggesting that during this very early stage of protostellar evolution the envelope mass-loss rate is dominated by gas infall onto the star-disk system (e.g., Ladd et al. 1998; Henriksen et al. 1997; Bontemps et al. 1996).

5.4. *Outflow-Envelope Interactions: An Empirical Model*

The widening of outflow cavities, the change in circumstellar envelope morphology and kinematics, and the decrease of circumstellar mass and mass-loss rate with source age all indicate that the protostellar outflow has a major role in the early stages of star formation, particularly in the evolution of the dense circumstellar envelope. Our data support the following empirical model of the evolution of outflow-envelope interactions (shown schematically in Fig. 8).

At very early stages of protostellar evolution, the young, powerful, and well-collimated outflow entrains and pushes on gas as it burrows through the envelope, altering the distribution and kinematics of dense gas. This interaction causes the elongated distribution of the dense gas, as traced by the $C^{18}O$ in our observations and a velocity gradient along the outflow axis on scales of 10^3 AU (see Fig. 8). At this early stage the envelope mass-loss rate is dominated by the infalling envelope gas onto the star-disk system.

With time, the envelope mass decreases, and the outflow cavities widen. This enables circumstellar gas at larger angles from the outflow axis to be entrained and cleared away by the outflow until eventually most of the dense circumstellar gas is concentrated outside the outflow cavities in structures perpendicular to the outflow axis, thereby decreasing the volume of the infalling region (see Fig. 8). At this stage most of the remaining dense circumstellar gas has not yet been perturbed by outflow motions, and the velocity structure of the envelope is dominated by either infall or rotation, depending on the age of the source (see Hogerheijde 2001). The outflow-envelope interaction is mainly traced by the ^{13}CO outflow emission, as the lower density in the outer envelope precludes the use of $C^{18}O$ as a probe. From this point (Class I and later) the mass-loss rate of the envelope is dominated by the outflow's clearing effect.

As the nascent star evolves further, the outflow lobes keep widening, and by the time the source reaches Class II status, most of the dense circumstellar envelope has been swept away by the outflow or has fallen into the circumstellar disk-star system. Only remnants of the original protostellar environment will be detectable (see Fig. 8). In some cases, gas that has been entrained by the outflow may form relatively dense shells and clumps at the edge of the outflow lobe, which can be observed in ^{13}CO and $C^{18}O$ emission around Class II sources (as seen in our sample and in Welch et al. 2000). We speculate that as the YSO evolves further and reaches the end of the Class II stage, the very wide outflow cavities will finish clearing the surrounding gas that is left, halting the infall process altogether.

5.5. *Outflow Chemistry*

Our multimolecular line observations also provide evidence that protostellar outflows can have a chemical impact on their envelope. As discussed in § 4.5 and shown in Table 7, we can estimate the HCO^+ abundance, X_{HCO^+}, in the outflow. Comparing our results with a "standard" abundance of $\sim 7 \times 10^{-9}$ (Jørgensen et al. 2004), we see that the HCO^+ abundance is clearly enhanced in the IRAS 3282 and HH 114mms outflows. In the case of L1228, the lower limit of X_{HCO^+} in the blue and red outflow lobes is similar to, and less than a factor of 2 less than, the "standard" HCO^+ abundance, respectively. In the case of RNO 43, the estimated X_{HCO^+} lower limit of the RNO 43 outflow is similar to

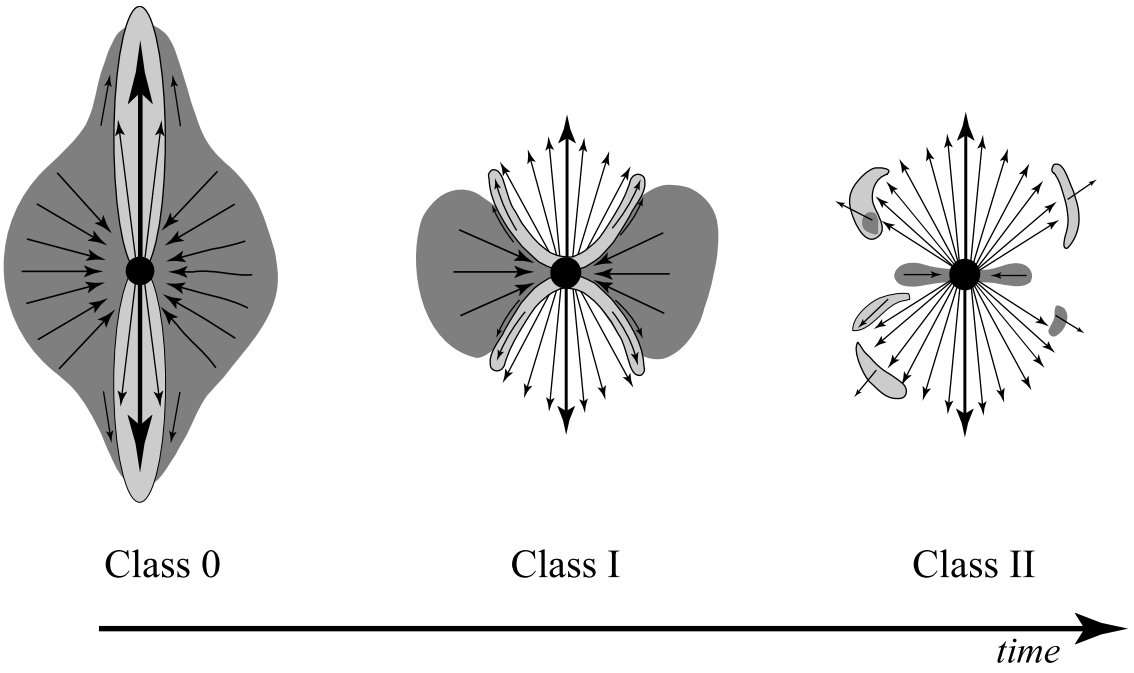

FIG. 8.—Schematic picture of outflow-envelope interaction evolution. Dark gray regions denote high-density (envelope) gas, mostly traced by $C^{18}O$ in our observations. Light gray regions show the molecular outflow traced by the ^{12}CO and ^{13}CO. Arrows indicate the gas motion. See § 5.4 for details.

the "average" HCO^+ abundance in envelopes around Class 0 sources found by Jørgensen et al. (2004). It is possible that in these two sources the HCO^+ abundance may be slightly enhanced, but our data are not sufficient to firmly make this conclusion. In the other sources in our sample, the HCO^+ is similar to, or below, the standard abundance.

The HCO^+ emission seen in Figure 3 arises mainly along the outflow cavity walls or the outflow lobes, and the observed overabundance is consistent with chemical models that predict HCO^+ enhancement in outflow walls due to the shock-triggered release of molecules from dust mantles and subsequent chemical reactions in the warm gas (Rawlings et al. 2000, 2004; Viti et al. 2002). Hence, it is clear that some of the sources in our sample power outflows that are affecting the chemical composition of their surroundings. On the other hand, HCO^+ outflows with abundances at or below the standard value must arise in dense ($n \gtrsim 10^3$) envelope gas (see Evans 1999) that has been entrained by the outflow, where shocks have not seriously affected the chemical properties of the environment. In some sources the HCO^+ outflow emission does not trace the entire extent of the outflow wall (e.g., HH 300 and L1228) or does not trace both outflow lobes (e.g., HH 114mms and RNO 43). This could result from differences in the environmental conditions, such as density, shock-induced radiation, or chemical composition, or in the effects of optical depth.

6. SUMMARY

Our systematic high angular resolution (3″–7″), multimolecular line survey of the circumstellar environment within $\sim 10^4$ AU of nine protostars at different evolutionary stages has enabled detailed studies of the kinematics, morphology, density distribution, and chemistry of the circumstellar gas. These in turn have permitted investigations of how the circumstellar envelopes and protostellar outflows change with time.

Our ^{12}CO images trace high-velocity outflowing molecular material around all sources. We detect a clear trend in the morphology of the protostellar molecular outflows. The youngest sources (Class 0) in our sample power molecular outflows with jetlike morphologies or cone-shaped lobes with opening angles less than 55°. The sightly more evolved (Class I) sources in our sample have molecular outflows with lobe opening angles of more than 75°. Outflows from the most evolved young stars in our sample, the Class II sources, have even wider lobes or no definite shape or structure. Combining our data with that from a number of sources in the literature shows that the outflow opening angle close to the source widens with time.

The denser, lower velocity gas probed by our ^{13}CO and HCO^+ observations appears to arise from the outflow cavity walls or very close to the protostar. We suggest that this is dense gas from the outer regions of the circumstellar envelope that has been entrained by the high-velocity flow, thereby eroding the envelope and helping to widen the outflow cavities. We also suggest that evolutionary changes in the morphology and velocity field of the dense circumstellar envelopes, detected in our $C^{18}O$ images, are mainly caused by outflow-envelope interactions. Class 0 source envelopes, for example, are elongated with velocity gradients along the outflow axis, indicating that the young and powerful protostellar outflows can entrain dense envelope gas. Class I envelopes, by contrast, are elongated more or less perpendicular to the outflow axis and concentrated outside the outflow lobes, as if most of the dense gas along the outflow axis has already been displaced. By the Class II stage the sparse $C^{18}O$ emission observed is constrained to the outflow lobe edges, consistent with most, if not all, of the dense gas being cleared.

Not unexpectedly, our results show a decrease in envelope mass as the age of the protostar increases. Comparisons of the estimated envelope mass-loss rate with the dense gas outflow rate imply that the protostellar outflow plays an important role in envelope mass loss during and after the Class I stage. For younger protostars, envelope mass loss is more likely to be dominated by large infall rates. Finally, enhanced abundance of HCO^+ in the outflow in some of the sources in our sample indicates that the chemical composition of the environment around these protostars is affected by shock-induced chemical processes in the outflow-envelope interface.

Taken together, these trends demonstrate that outflows from protostars have a major physical and chemical impact on their environments throughout the entire star formation process and are an integral part of that process. An understanding of their origins, evolution, and detailed characteristics is clearly critical for theories of star formation.

H. G. A. is supported by an NSF Astronomy and Astrophysics Postdoctoral Fellowship under award AST-0401568. The Owens Valley Radio Observatory millimeter array is supported by the NSF grant AST-0228955. We are grateful to Chin-Fei Lee, Mario Tafalla, and Jennifer Hatchell for sharing their single-dish data with us.

APPENDIX

DESCRIPTION OF SOURCES

A1. HH 114mms

The HH 114mms protostar is a Class 0 source in L1589, a cloud in the western part of the λ Orionis molecular shell. It was first detected at 1.3 mm (Chini et al. 1997) and has also been observed at 3.6 cm (Rodríguez & Reipurth 1996). The ^{12}CO (1–0) map of the nearby HH 114/115 molecular outflow by Lee et al. (2002) partially overlaps the blue lobe of the HH 114mms CO outflow. Our data show the HH 114mms CO outflow is highly collimated, with a small bend in both outflow lobes about 7″ away from the source, where the outflow axis appears to change direction. This morphology may indicate that the axis of the underlying protostellar wind has changed over time. CO channel maps show that in both outflow lobes the highest velocity gas is concentrated farthest from the source. In addition, the opening angle of the CO blue lobe widens slightly at lower outflow velocities, rather like the HH 211 outflow (Gueth & Guilloteau 1999). The morphology and velocity distribution of the outflowing gas suggests that an underlying jetlike wind drives the molecular outflow.

A2. RNO 43

A detailed study of the RNO 43 molecular outflow, the circumstellar envelope, and the outflow-envelope interactions within 2×10^4 AU of the protostar is presented in Paper II. This outflow lies in the L1582B dark cloud at a distance of about 460 pc, in the λ Orionis ring (Bence et al. 1996). The outflow arises from IRAS 05295+1247, a deeply embedded Class 0 source that has been observed from far-infrared to centimeter wavelengths (Cohen et al. 1985; Beichman et al. 1986; Zinnecker et al. 1992; Reipurth et al. 1993; Anglada et al. 1992; Chini et al. 1997). The 3.4 pc long RNO 43 optical outflow includes four major Herbig-Haro (HH) knots, HH 243, HH 244, HH 245, and HH 179 (Cohen 1980; Reipurth et al. 1997). The large-scale molecular (CO) outflow extends about half a degree ($\sim$4 pc) on the sky (Cabrit et al. 1988; Bence et al. 1996). The positions of the HH knots and the morphology of the giant molecular outflow indicate that the axis of the RNO 43 flow has changed over time (Bence et al. 1996; Reipurth et al. 1997).

A3. IRAS 3282

Single-dish ^{12}CO (2–1) observations of the environment surrounding IRAS 3282 by Bachiller et al. (1991) revealed a young, 0.5 pc long, fast, and highly collimated bipolar molecular outflow. The high-velocity outflow ($\sim$50 km s^{-1}) gas has a jetlike morphology, while the slower ($\sim$10 km s^{-1}) component exhibits wider outflow lobes. Observations of the ammonia core suggest that the dense core gas is being accelerated along the outflow cavity walls (Tafalla et al. 1993). High-resolution OVRO observations of the 1.3 mm dust continuum reveal that IRAS 3282 is a binary source with a 420 AU separation and a mass ratio of 0.2 (Launhardt 2004). Our ^{12}CO (1–0) data show that at outflow velocities between about 2 and 7 km s^{-1} both lobes have a V-shaped morphology, consistent with a jet bow shock entrainment model (e.g., Gueth et al. 1996; Gueth & Guilloteau 1999).

A4. HH 300

IRAS 04239+2436, the source of the HH 300 outflow, is located in the westernmost region of the B18 cloud (sometimes referred as the B18w region) in the Taurus molecular cloud complex. Infrared photometry and spectra indicate that the source is a deeply embedded Class I protostar (Myers et al. 1987; Greene & Lada 1996). Dust continuum emission surrounding the source was mapped at 1.3 mm (at $\sim$12″ resolution) by Motte & André (2001). The HH 300 optical outflow is about 1.2 pc long and comprises three different HH knots (Reipurth et al. 1997). The density, velocity, and momentum distribution of the large-scale molecular outflow indicates that it is driven by an underlying precessing, episodic wind (Arce & Goodman 2001). *HST* images at 1.644 and 2.122 μm by Reipurth et al. (2000) indicate that IRAS 04239+2436 is a binary source. In addition, they reveal the existence of a parabolic nebula with a small (1000 AU) jet along its symmetry axis, northeast of the source (i.e., the blueshifted side of the outflow). In our ^{12}CO images, the blue and red molecular outflow lobes have shapes and orientations similar to those of the near-infrared parabolic nebula.

A5. L1228

A detailed study of the infalling envelope, the wide-angle L1228 molecular outflow, and its impact on the circumstellar envelope is presented in Paper I. This outflow is named after its parent molecular cloud, located in the Cepheus flare cloud complex at a distance of 200 pc (Kun 1998). The outflow source, IRAS 20582+7724, is an embedded (Class I) low-luminosity protostar associated with a $\sim$1 pc–long bipolar molecular outflow, first observed in CO (1–0) by Haikala & Laureijs (1989). IRAS 20582+7724 also powers a $\sim$1.5 pc–long optical flow, HH 199 (Bally et al. 1995). The single-dish, multimolecular line study by Tafalla & Myers

(1997) indicates that the dense core gas is being disrupted by the L1228 outflow. The tentative detection of a binary companion is reported in Paper I.

A6. RNO 129

RNO 129 is located about 1° north of the L1228 core and is believed to be associated with the same cloud (Kun 1998). The protostellar source associated with the RNO 129 nebulosity is IRAS 21004+7811 (Ogura & Sato 1990). An extensive recent study of the region by Movsessian & Magakian (2004) presents optical images of the RNO 129 nebulosity and the HH objects near it and concludes that the central star is a binary that powers a collimated (optical) outflow. Here we show the first maps of the molecular outflow associated with RNO 129.

A7. RNO 91

RNO 91 and its source, IRAS 16316−1540, are located in the L43 cloud, part of the ρ Ophiuchi molecular cloud complex at a distance of about 160 pc. Optical, CO, CS, and NH_3 observations of the core suggest that the molecular outflow has blown through the dense gas, creating a cavity south of the outflow source (Mathieu et al. 1988). Based on single-dish and interferometer maps at higher angular resolution, the molecular outflow has been successfully modeled as a slowly expanding shell driven by a wide-angle wind (Bence et al. 1998; Lee et al. 2000, 2001; Lee & Ho 2005). Given the large width of the outflow near its base, about 10^4 AU, our observations, which are limited to regions within about 6.5×10^3 AU of the source, do not show the full impact of the RNO 91 outflow on the surrounding envelope. Fortunately, the mosaic of interferometer observations by Lee & Ho (2005), which cover the surrounding environment within at least 10^4 AU of IRAS 16316−1540, shows these outflow-envelope interactions.

A8. T Tau

The T Tau binary system comprises the optically visible star T Tau N and an infrared companion, T Tau S, separated by only 0.″7. Both binary elements are known outflow sources. The outflow most likely driven by T Tau S has an approximately northwest axis (e.g., Solf & Böhm 1999; Reipurth et al. 1997 and references therein), while the other, seen nearly pole-on, with a northeast-southwest or east-west axis, is most likely driven by T Tau N (Solf & Böhm 1999; Momose et al. 1996 and references therein). It is generally accepted that both T Tau N and T Tau S are of similar age; T Tau N is optically visible because its light can escape through the nearly pole-on outflow cavity walls (e.g., Momose et al. 1996), while T Tau S is obscured by an envelope or the outer parts of T Tau N's disk and is highly reddened (e.g., Hogerheijde et al. 1997b). However, the bolometric temperatures of the two stars are extremely different: 501 and 3452 K for T Tau S and T Tau N, respectively (Chen et al. 1995). Since we do not have separate bolometric temperature measurements for each element of other close ($<5''$) binary systems in our sample (i.e., IRAS 3282, HH 300, L1228, and RNO 129) and since T Tau S and T Tau N should be coeval, we adopt a single $T_{\rm bol}$ for both stars using flux measurements at different wavelengths that do not resolve the binary companions.

The molecular gas morphology and kinematics in the region surrounding T Tau are quite complex, and different observational studies offer different interpretations. Weintraub et al. (1989b) conducted the first interferometer observations (with a beam of $\sim 6''$) of the ^{12}CO (1–0) and ^{13}CO (1–0) surrounding T Tau and interpreted their observations to show a circumstellar Keplerian disk. The combined interferometer and single-dish ^{13}CO (1–0) observations of Momose et al. (1996) show a different picture and were interpreted to show biconical outflowing shells. The interpretation by Schuster et al. (1997), based on their single-dish ^{12}CO (3–2) and C^{18}O (2–1) observations (with beams of 12–14″), is similar to that of Momose et al. (1996), but they claim that more than one outflow is needed to explain the observed gas morphology and kinematics. Observations of the extended molecular hydrogen in the $v = 1$–0 $S(1)$ line show the emission appears to arise from a precessing jet in an approximate north-south axis powered by T Tau S (van Langevelde et al. 1994b). Interferometer observations of the HCO^+ (1–0) toward T Tau show possible evidence of an infalling circumstellar envelope (van Langevelde et al. 1994a).

The OVRO ^{12}CO (1–0) maps presented here are much more sensitive and have a better angular resolution (by a factor of 2) and better u-v coverage (by a factor more than 4) than those presented by Weintraub et al. (1989b). Our data do not show the Keplerian circumstellar disk suggested by Weintraub et al. (1989b). Instead, at velocities far away from the cloud velocity (i.e., $v_{\rm LSR} \lesssim 6.5$ km s^{-1} and $v_{\rm LSR} \gtrsim 9.5$ km s^{-1}) the ^{12}CO emission shows outflow lobes with an east-west or northeast-southwest axis, consistent with the Momose et al. (1996) picture—where most of the outflowing molecular emission comes from an outflow powered by T Tau N.

Close to the cloud velocity the ^{12}CO emission (not shown here) is complex and extended, and it is clear that we are missing a substantial amount of flux. Our ^{13}CO, C^{18}O, and HCO^+ maps are consistent with the lower angular resolution maps presented by Momose et al. (1996), Schuster et al. (1997), and van Langevelde et al. (1994a), respectively.

A9. GK/GI Tau

GK Tau and GI Tau are two classical T Tauri stars located in the B18 cloud in Taurus that are only separated by 13″ ($\sim$1820 AU). In addition, GK Tau has a faint companion only 2.″5 (350 AU) away (Reipurth & Zinnecker 1993). Estimates of the age and bolometric temperature for GI Tau and GK Tau indicate that these stars are coeval (Hartigan et al. 1994; Chen et al. 1995). Here we assume a common bolometric temperature of 2700 K. Aspin & Reipurth (2000) detected several HH knots near the triple system and were able to determine that GK Tau (or its faint companion) is the driving source of at least some of the HH knots. Their observations also reveal that the entire triple system is surrounded by a common envelope of reflection nebulosity. Our CO maps of the region are the first to show the molecular outflow associated with the GK/GI system.

REFERENCES

André, P., Ward-Thompson, D., & Barsony, M. 2000, in Protostars and Planets IV, ed. V. Mannings, A. Boss, & S. Russell (Tucson: Univ. Arizona Press), 59
Anglada, G., Rodriguez, L. F., Canto, J., Estalella, R., & Torrelles, J. M. 1992, ApJ, 395, 494
Arce, H. G., & Goodman, A. A. 2001, ApJ, 554, 132
———. 2002, ApJ, 575, 911
Arce, H. G., & Sargent, A. I. 2004, ApJ, 612, 342 (Paper I)
———. 2005, ApJ, 624, 232 (Paper II)
Aspin, C., & Reipurth, R. 2000, MNRAS, 311, 522
Bachiller, R., Guilloteau, S., Dutrey, A., Planesas, P., & Martín-Pintado, J. 1995, A&A, 299, 857
Bachiller, R., Martín-Pintado, J., & Planesas, P. 1991, A&A, 251, 639
Bally, J., Devine, D., Fesen, R. A., & Lane, A. P. 1995, ApJ, 454, 345
Beckwith, S. V. W., & Sargent, A. I. 1991, ApJ, 381, 250
Beckwith, S. V. W., Sargent, A. I., Scoville, N. Z., Masson, C. R., Zuckerman, B., & Phillips, T. G. 1986, ApJ, 309, 755
Beckwith, S. V. W., Steven, V. W., Sargent, A. I., Chini, R. S., & Guesten, R. 1990, AJ, 99, 924
Beichman, C. A., Myers, P. C., Emerson, J. P., Harris, S., Mathieu, R., Benson, P. J., & Jennings, R. E. 1986, ApJ, 307, 337
Beltrán, M. T., Gueth, F., Guilloteau, S., & Dutrey, A. 2004, A&A, 416, 631
Bence, S. J., Padman, R., Isaak, K. G., Wiedner, M. C., & Wright, G. S. 1998, MNRAS, 299, 965
Bence, S., Richer, J. S., & Padman, R. 1996, MNRAS, 279, 866
Bontemps, S., Andre, P., Terebey, S., & Cabrit, S. 1996, A&A, 311, 858
Buckle, J. V., & Fuller, G. A. 2002, A&A, 381, 77
Cabrit, S., Goldsmith, P. F., & Snell, R. L. 1988, ApJ, 334, 196
Chen, H., Myers, P. C., Ladd, E. F., & Wood, D. O. S. 1995, ApJ, 445, 377
Chini, R., Reipurth, B., Sievers, A., Ward-Thompson, D., Haslam, C. G. T., Kreysa, E., & Lemke, R. 1997, A&A, 325, 542
Cohen, M. 1980, AJ, 85, 29
Cohen, M., Harvey, P. M., & Schwartz, R. D. 1985, ApJ, 296, 633
Delamarter, G., Frank, A., & Hartmann, L. 2000, ApJ, 530, 923
Dent, W. R. F., Matthews, H. E., & Ward-Thompson, D. 1998, MNRAS, 301, 1049
Evans, N. J. 1999, ARA&A, 37, 311
Frerking, M. A., Langer, W. D., & Wilson, R. W. 1982, ApJ, 262, 590
Fuller, G. A., & Ladd, E. F. 2002, ApJ, 573, 699
Greene, T. P., & Lada, C. J. 1996, ApJ, 461, 345
Gueth, F., & Guilloteau, S. 1999, A&A, 343, 571
Gueth, F., Guilloteau, S., & Bachiller, R. 1996, A&A, 307, 891
Gueth, F., Guilloteau, S., Dutrey, A., & Bachiller, R. 1997, A&A, 323, 943
Haikala, L. K., & Laureijs, R. J. 1989, A&A, 223, 287
Hartigan, P., Strom, K. M., & Strom, S. E. 1994, ApJ, 427, 961
Hatchell, J., Richer, J. S., Fuller, G. A., Qualtrough, C. J., Ladd, E. F., & Chandler, C. J. 2005, A&A, 440, 151
Henning, Th., & Launhardt, R. 1998, A&A, 338, 223
Henriksen, R., André, P., & Bontemps, S. 1997, A&A, 323, 549
Herbig, G. H., & Bell, K. R. 1988, Lick Obs. Bull., 1111
Hogerheijde, M. R. 2001, ApJ, 553, 618
Hogerheijde, M. R., van Dishoeck, E. F., Blake, G. A., & van Langevelde, H. J. 1998, ApJ, 502, 315
Hogerheijde, M. R., van Langevelde, H. J., Mundy, L. G., Blake, G. A., & van Dishoeck, E. F. 1997a, ApJ, 490, L99
———. 1997b, ApJ, 489, 293
Jijina, J., Myers, P. C., & Adams, F. C. 1999, ApJS, 125, 161
Jørgensen, J. K., Hogerheijde, M. R., Blake, G. A., van Dishoeck, E. F., Mundy, L. G., & Schöier, F. L. 2004, A&A, 415, 1021
Königl, A., & Pudritz, R. E. 2000, in Protostars and Planets IV, ed. V. Mannings, A. P. Boss, & S. S. Russell (Tucson: Univ. Arizona Press), 759
Kun, M. 1998, ApJS, 115, 59
Kwan, J., & Tademaru, E. 1995, ApJ, 454, 382
Lada, C. J. 1999, in The Origin of Stars and Planetary Systems, ed. C. J. Lada & N. D. Kylafis (Dordrecht: Kluwer), 143
Ladd, E. F., Fuller, G. A., & Deane, J. R. 1998, ApJ, 495, 871
Langer, W. D., & Penzias, A. A. 1993, ApJ, 408, 539
Langer, W. D., Velusamy, T., & Xie, T. 1996, ApJ, 468, L41
Launhardt, R. 2004, in IAU Symp. 221, Star Formation at High Angular Resolution, ed. M. Burton, R. Jayawardhana, & T. Bourke (San Francisco: ASP), 213
Lee, C.-F., & Ho, P. T. P. 2005, ApJ, 624, 841
Lee, C.-F., Mundy, L. G., Reipurth, B., Ostriker, E. C., & Stone, J. M. 2000, ApJ, 542, 925
Lee, C.-F., Mundy, L. G., Stone, J. M., & Ostriker, E. C. 2002, ApJ, 576, 294
Lee, C.-F., Stone, J. M., Ostriker, E. C., & Mundy, L. G. 2001, ApJ, 557, 429
Looney, L. W., Mundy, L. G., & Welch, W. J. 2000, ApJ, 529, 477
Masson, C. R., & Chernin, M. L. 1993, ApJ, 414, 230
Mathieu, R. D., Myers, P. C., Schild, R. E., Benson, P. J., & Fuller, G. A. 1988, ApJ, 330, 385
Matt, S., Winglee, R., & Böhm, K.-H. 2003, MNRAS, 345, 660
Matzner, C. D., & McKee, C. F. 2000, ApJ, 545, 364
Mizuno, A., Onishi, T., Yonekura, Y., Nagahama, T., Ogawa, H., & Fukui, Y. 1995, ApJ, 445, L161
Momose, M., Ohashi, N., Kawabe, R., Hayashi, M., & Nakano, T. 1996, ApJ, 470, 1001
Momose, M., Ohashi, N., Kawabe, R., Nakano, T., & Hayashi, M. 1998, ApJ, 504, 314
Motte, F., & André, P. 2001, A&A, 365, 440
Movsessian, T. A., & Magakian, T. Yu. 2004, Astron. Rep., 48, 988
Myers, P. C., Fuller, G. A., Mathieu, R. D., Beichman, C. A., Benson, P. J., Schild, R. E., & Emerson, J. P. 1987, ApJ, 319, 340
Myers, P. C., & Ladd, E. F. 1993, ApJ, 413, L47
Ogura, K., & Sato, F. 1990, PASJ, 42, 583
Ohashi, N., Hayashi, M., Ho, P. T. P., & Hirano, N. 1996, ApJ, 466, 957
Ohashi, N., Hayashi, M., Ho, P. T. P., & Momose, M. 1997, ApJ, 475, 211
Raga, A. C., & Cabrit, S. 1993, A&A, 278, 267
Rawlings, J. M. C., Redman, M. P., Keto, E., & Williams, D. A. 2004, MNRAS, 351, 1054
Rawlings, J. M. C., Taylor, S. D., & Williams, D. A. 2000, MNRAS, 313, 461
Reipurth, B., Bally, J., & Devine, D. 1997, AJ, 114, 2708
Reipurth, B., Chini, R., Krügel, E., Kreysa, E., & Sievers, A. 1993, A&A, 273, 221
Reipurth, B., Yu, K. C., Heathcote, S., Bally, J., & Rodríguez, L. F. 2000, AJ, 120, 1449
Reipurth, B., & Zinnecker, H. 1993, A&A, 278, 81
Richer, J., Shepherd, D., Cabrit, S., Bachiller, R., & Churchwell, E. 2000, in Protostars and Planets IV, ed. V. Mannings, A. P. Boss, & S. S. Russell (Tucson: Univ. Arizona Press), 867
Rodríguez, L. F., & Reipurth, B. 1996, Rev. Mex. AA, 32, 27
Sault, R. J., Teuben, P. J., & Wright, M. C. H. 1995, in ASP Conf. Ser. 77, Astronomical Data Analysis Software and Systems IV, ed. R. A. Shaw, H. E. Payne, & J. J. E. Hayes (San Francisco: ASP), 433
Schuster, K.-F., Harris, A. I., & Russell, A. P. G. 1997, A&A, 321, 568
Scoville, N. Z., Carlstrom, J. E., Chandler, C. J., Phillips, J. A., Scott, S. L., Tilanus, R. P. J., & Wang, Z. 1993, PASP, 105, 1482
Shang, H., Shu, F. H., & Glassgold, A. E. 1998, ApJ, 493, L91
Shu, F. H., Najita, J. R., Shang, H., & Li, Z.-Y. 2000, in Protostars and Planets IV, ed. V. Mannings, A. P. Boss, & S. S. Russell (Tucson: Univ. Arizona Press), 789
Solf, J., & Böhm, K.-H. 1999, ApJ, 523, 709
Tafalla, M., Bachiller, R., Martín-Pintado, J., & Wright, M. C. H. 1993, ApJ, 415, L139
Tafalla, M., & Myers, P. C. 1997, ApJ, 491, 653
Terquem, C., Eislöffel, J., Papaloizou, J. C. B., & Nelson, R. P. 1999, ApJ, 512, 131
Torrelles, J. M., Gómez, F. F., & Anglada, G. 1995, RevMexAA Ser. Conf., 1, 149
van Langevelde, H. J., van Dishoeck, E. F., & Blake, G. A. 1994a, ApJ, 425, L45
van Langevelde, H. J., van Dishoeck, E. F., van der Werf, P. P., & Blake, G. A. 1994b, A&A, 287, L25
Velusamy, T., & Langer, W. D. 1998, Nature, 392, 685
Viti, S., Natarajan, S., & Williams, D. A. 2002, MNRAS, 336, 797
Weintraub, D. A., Masson, C. R., & Zuckerman, B. 1987, ApJ, 320, 336
Weintraub, D. A., Sandell, G., & Duncan, W. D. 1989a, ApJ, 340, L69
Weintraub, D. A., Zuckerman, B., & Masson, C. R. 1989b, ApJ, 344, 915
Welch, W. J., Hartmann, L., Helfer, T., & Briceño, C. 2000, ApJ, 540, 362
Wilkin, F. P., & Stahler, S. W. 2003, ApJ, 590, 917
Wiseman, J., Wootten, A., Zinnecker, H., & McCaughrean, M. 2001, ApJ, 550, L87
Yu, K. C., Billawala, Y., & Bally, J. 1999, AJ, 118, 2940
Zinnecker, H., Bastien, P., Arcoragi, J.-P., & Yorke, H. W. 1992, A&A, 265, 726